https://doi.org/10.5194/egusphere-2026-2835
Preprint. Discussion started: 2 June 2026

Modelling and Parameterisation of Ice-Shelf Melting in the Amundsen Sea, Antarctica

Paul R. Holland[1], Adrian Jenkins[2], David T. Bett[1], and Suzanne L. Bevan[3]

[1]British Antarctic Survey, Cambridge, UK
[2]Northumbria University, Newcastle, UK
[3]Swansea University, Swansea, UK

Correspondence to: Paul R. Holland (p.holland@bas.ac.uk)

Abstract. Ice loss from the Amundsen Sea sector of West Antarctica is a major contributor to global sea-level rise, and is a key source of uncertainty in projections of sea level over the coming centuries. This ice loss is ultimately driven by changes in ocean melting, which must therefore be represented in ice-sheet model forecasts. In this study we use high-resolution ocean simulations to understand the mechanisms controlling ice-shelf melting in the eastern Amundsen Sea. Melting is focussed on four 'hot spots' of melting of the deep ice where the main glacier trunks cross the grounding line. Secondary areas of elevated melting occur beneath the associated buoyant 'meltwater outflows', which are guided by ice topography and Coriolis force. The simulations are then used to test simple local parameterisations of melting. The best parameterisation expresses melt rate as a simple function of ocean temperature to the power 3/2, ice slope to the power 1/2, and tapered to zero near the grounding line. This matches the simulated melting with r^2=0.65, capturing melting hot spots near the grounding line but failing to represent melting along meltwater outflow paths. This parameterisation also broadly captures the strong melting feedbacks that appear when the model is applied to possible future ice geometries. It is possible that simple local melting parameterisations may be sufficient wherever ice shelf buttressing is focussed near the grounding line (such as Thwaites Glacier), but may be inadequate in regions where melting beneath shear margins controls buttressing (such as Pine Island Glacier).

1 Introduction

The West Antarctic Ice Sheet is losing ice, contributing to sea-level rise (Rignot et al., 2019; Shepherd et al., 2019; Otosaka et al., 2023). This ice loss is focussed on the Amundsen Sea sector, where changes in ocean melting have led to thinning, retreat, and increased damage of the floating ice shelves and acceleration and thinning of their tributary glaciers (e.g. Shepherd et al., 2004; Mouginot et al., 2014; Konrad et al., 2017; Lhermitte et al., 2020). The continental shelf sea in the Amundsen Sea is flooded with a layer of warm (+1°C) Circumpolar Deep Water from the deep Southern Ocean, and variability in this warm layer controls ice melting rates (Dutrieux et al., 2014; Jenkins et al., 2018). The ice loss has been caused by some combination of historical anthropogenic change in this Circumpolar Deep Water layer (Naughten et al., 2022; Turner et al., 2025) and natural ocean variability (Smith et al., 2017; Holland et al., 2022; O'Connor et al., 2023), enhanced by ice and ocean feedbacks (De Rydt et al., 2014; Favier et al., 2014; Joughin et al., 2014; Lhermitte et al., 2020; Holland et al., 2023; Reed et al., 2024). The future evolution of oceanic melting of ice shelves in this region is a key control over projections of sea-level rise (Arthern and Williams, 2017; Naughten et al., 2023; Seroussi et al., 2023).

Despite the importance of ocean melting of ice shelves in the Amundsen Sea, our understanding of the melting patterns and their underlying oceanic physics remains incomplete. Overall melting rates can be derived from oceanographic measurements (Dutrieux et al., 2014; Jenkins et al., 2018), but this offers no insight into the controls over spatial patterns of melting, which are important to the glacier dynamical response to ice thinning (Morlighem et al., 2021; Naughten et al., 2023). Melting patterns can be estimated from ice thickness and velocity fields derived from remote sensing (Dutrieux et al., 2013; Shean et al., 2019; Zinck et al., 2023; Chartrand et al., 2024; Gourmelen et al., 2025; Lowery et al., 2025; Zinck et al., 2026), but this can be inaccurate in areas where the ice is not a continuum, contains small-scale thickness variations, or is not freely floating. Furthermore, no oceanographic process information is available to accompany these maps. More information can be gained about the ocean processes controlling melting by using high-resolution ocean models, which are now being applied to Amundsen Sea ice shelves at a resolution capable of resolving the detailed processes and topographic features that control melting (Dutrieux et al., 2014; Nakayama et al., 2019; Nakayama et al., 2021; Holland et al., 2023; Lambert et al., 2023; Gourmelen et al., 2025; Lowery et al., submitted).

The need to improve our understanding of ice shelf melting in this region has an important practical implication: The need to constrain projections of the future ice-sheet contribution to sea-level rise. The future trajectory of the West Antarctic Ice Sheet offers the greatest source of uncertainty in projections of global sea-level rise (IPCC, 2021). Of this uncertainty, the future evolution of ocean melting is a leading source (Seroussi et al., 2023). Running coupled ice—ocean models is widely considered the most accurate approach to obtaining future melt rates, because this accounts for the effect of changing ice shelf geometry on melt rates (Seroussi et al., 2017; Bett et al., 2024; De Rydt and Naughten, 2024). However, developing and running coupled ice-ocean models is technically demanding, and the ocean model usually demands most of the computational time in the coupled system. A far more common approach is to use simple parameterisations of ice-shelf melting to drive stand-alone ice-sheet models, freeing up resources for studies of ice model uncertainty and probabilistic forecasting (Nias et al., 2019; Seroussi et al., 2023; Coulon et al., 2024). Increased understanding of the strengths and weaknesses of these melt parameterisations, relative to coupled ice—ocean modelling, could provide better constraint over future projections of ice loss from the Amundsen Sea sector.

A wide hierarchy of parameterisations have been applied to ice-shelf melting in the Amundsen Sea, from simple local functions of depth or temperature (Jourdain et al., 2020; Joughin et al., 2021; Reed et al., 2024), to one-dimensional (horizontal) patterns derived from plume theory (Lazeroms et al., 2019), to quasi-two-dimensional (vertical) box models (Olbers and Hellmer, 2010; Reese et al., 2018a), to two-dimensional (horizontal) layer models (Payne et al., 2007; Lambert et al., 2023). Machine learning approaches to melting parameterisation are also now being developed (Burgard et al., 2023; Rosier et al., 2023). However, there are only a few studies examining the relative merits of these different approaches. For example, De Rydt and Gudmundsson (2016) and Snow et al. (2017) show that simple depth-dependent parameterisations do not reproduce the results of coupled ice—ocean models when applied to simple domains reminiscent of Amundsen Sea ice shelves. Favier et al. (2019) tested a wide range of parameterisations against a coupled ice—ocean model. For warm conditions reminiscent of the Amundsen Sea, they found that only formulations expressing melt rates as a quadratic function of ocean temperature were able to represent melt rate patterns and the melt sensitivity to warming. Burgard et al. (2022) and Burgard et al. (2023) extended this approach by using circum-Antarctic ocean simulations as their parameterisation target, finding that melt rate formulations based on plume theory and quadratic functions of temperature performed best in general, particularly in the Amundsen Sea, including in ocean warming scenarios. Lambert and Burgard (2025) found that the quadratic parameterisation had the highest sensitivity of melting to ocean warming, particularly in the deep warm waters of the Amundsen Sea.

The present study has two over-arching goals: i) to model ice—ocean interactions in the Amundsen Sea at high resolution and understand the ocean processes controlling melting and ii) to use these simulations as a model testbed to develop and test parameterisations of melting that could be used to force an ice-sheet model. The study complements previous assessments (Burgard et al., 2022; Burgard et al., 2023) by focussing solely on Amundsen Sea processes, at much higher resolution. First, we simulate present-day ocean conditions in the Amundsen Sea at high resolution. Next, we derive a set of local melting parameterisations and calibrate and validate these against the present-day simulations. Finally, we test the accuracy of these trained parameterisations in reproducing simulated melting using potential future, significantly retreated ice geometries (Bett et al., 2024). This provides insight into the parameterisations' performance when confronted with geometries outside their training dataset, and how well they capture the important coupled geometric ice—ocean feedbacks that influence future ice retreat in this region (Bett et al., 2024; De Rydt and Naughten, 2024). It is of course impossible to test all possible parameterisation approaches, so the model simulations are freely available for others to develop and test alternative parameterisations, or for general use in understanding Amundsen Sea ice—ocean interactions.

2 Methods

2.1 Modelling

2.1.1 Model setup

This study uses the MITgcm ocean model to solve the hydrostatic Boussinesq Navier-stokes equations in a small ocean domain covering the south-eastern Amundsen Sea shelf and its ice shelves, from Dotson Ice Shelf to PIG (Fig. 1). The model is deliberately simplified. It includes static floating ice shelves that are thermodynamically coupled to the ocean (Losch,

2008) but uses idealised climatic forcings (see below) and does not include a sea-ice model, tides, or subglacial outflows. The model setup follows the simulations of Holland et al. (2023) except for a coarsening of the horizontal grid, such that the model resolution is 400 m in the horizontal by 10 m in the vertical, with the model timestep unchanged at 30 s. These changes required an increase in the horizontal viscosity to maintain numerical stability, following the formula $A_h = 0.01\,(\Delta x)^2/(4\,\Delta t)$. All other mixing and melting parameters are identical to Holland et al. (2023).

The modelling strategy is to initialise the ocean domain with conditions reflective of cold, fresh Winter Water, then apply restoring boundary conditions that contain a deep layer of warm, salty Circumpolar Deep Water, and spin the model up as this water floods into the domain, until a steady state is achieved where the warming and salting from the boundary restoring balances the cooling and freshening from ice shelf melting. This is achieved after two years of simulation. We consider 6 model experiments: a reference contemporary simulation using ocean conditions and ice geometry representative of the present day, and a set of five future simulations that use successive time-slices of projected ice geometry from the coupled model of Bett et al. (2024). Details of the model geometry and forcings are presented below.

2.1.2 Ice and seabed geometries

It is important that we use the most accurate seabed and ice draft topography datasets, since we are focussed on the supply of ocean heat to the ice cavities, and the ocean currents that drive melting. For seabed bathymetry, we assemble our final dataset from several sources. First we lay down the seabed from BedMachine version 3 (Morlighem et al., 2020), then over-print this with the latest gridded ship swath bathymetry data (Frank Nitsche, personal communication 2023), a seabed dataset from submarine data beneath Pine Island Glacier (Dutrieux et al., 2014), and a seabed dataset beneath Dotson—Crosson and Thwaites ice shelves from constrained airborne gravimetry data (Jordan et al., 2020). This bathymetry dataset is used in all simulations.

In the reference present-day simulation, ice shelf draft is calculated from the ice surface elevation in the global 30-metre resolution Digital Elevation Model (DEM) from TanDEM-X data (González et al., 2020). For Thwaites Ice Shelf, this is over-printed using the final 2022 surface DEM from Holland et al. (2023). Ice draft is calculated from this combined surface DEM by assuming the ice is freely floating, using the EIGEN-6C4 geoid, a Dynamic Ocean Topography of 1.81 m, a firn-air thickness of 12 m, and ice and ocean densities of 917 and 1028 kg / m^3 respectively. The grounding line is determined to be wherever the floatation ice draft meets the seabed dataset. Near the grounding line the ice shelf is not expected to be in floatation, so within 2.5 ice thicknesses (a typical ice bending length scale) of any grounded ice, the ice shelf draft is deleted and replaced by linear interpolation between the remaining floating ice and grounded ice drafts.

In the future simulations we derive a floatation ice draft from the ice thickness generated by the simulations of Bett et al. (2024), and then repeat the above procedure to determine the grounding line and nearby ice draft. We use the ‘WARM’

https://doi.org/10.5194/egusphere-2026-2835
Preprint. Discussion started: 2 June 2026

experiment of Bett et al. (2024), which is forced by prescribing idealised warm ocean boundary conditions in the coupled model, and we choose to perform five time-slice experiments at $t = \{36, 72, 108, 144, 180\}$ years, corresponding to the ice states shown in Figs. 3 and 8 of Bett et al. (2024). With the warm forcing used in that study, after 180 years of coupled evolution these ice geometries represent a state in which Pine Island, Thwaites, Smith, and Kohler glaciers have all suffered extreme thinning and retreat.

2.1.3 Ocean forcing

In contrast to the complex regional topography used in the model, the ocean forcing is deliberately kept as simple as possible. We neglect all surface stresses and fluxes of heat and salt, and simply treat the open-ocean lateral boundaries on the northern and western edges of the domain (Fig. 1) as solid walls at which ocean properties are restored to a single idealised profile, uniform along the boundary. Similar to many previous studies, the profile features a warm (+1.2°C) and saline (34.7 psu) deep Circumpolar Deep Water layer below 700 m depth, with a colder (−1°C) and fresher (34 psu) Winter Water layer above 300 m depth, and thermocline in between. This corresponds to average present-day summertime ocean conditions in the eastern Amundsen Sea, central to the range of conditions used in previous studies (e.g. De Rydt et al., 2014; Holland et al., 2023). The restoring region is prescribed to be 20 grid cells (8 km) wide, with a restoring timescale that increases linearly into the domain from a value of 1 day on the boundary cells, to no restoring on the 20th grid cell.

The decision to use such idealised ocean forcings is highly influential and should be borne in mind when interpreting the results. This choice neglects several important features of the regional oceanography, such as cooler water in Dotson Trough (Jacobs et al., 2012; Jenkins et al., 2018), the meridional circulation in the eastern Amundsen Sea that brings the warmest Circumpolar Deep Water towards the ice shelves (Nakayama et al., 2013; Kimura et al., 2017), cooling in polynyas (St-Laurent et al., 2015; Bett et al., 2020), and local wind-driven gyres (Thurnherr et al., 2014; Zheng et al., 2022). The choice is motivated by the aims of our study. To understand the sub-ice-shelf ocean processes governing melting, we choose to isolate those processes from other influences external to the sub-ice cavities. To test parameterisations of melting, we choose an experimental testbed that reflects the expected parameterisation usage cases. Parameterisations are usually driven by a temperature profile from offshore of the ice shelves (Jourdain et al., 2020; Burgard et al., 2022), so using a single boundary forcing profile provides a clear choice for this input. Furthermore, if we were to use any model with full regional complexity, this complexity would be locked into the parameterisation by our calibration and validation procedure. It may not be appropriate to preserve these details under changing climatic and ice geometry conditions, and these details may also conflict with the usage case. For example, if we implicitly include the effects of polynyas in a melting parameterisation, and then future studies drive this parameterisation with a model that includes polynyas, the polynyas would be incorporated twice. Thus, with our idealised forcing we seek only to parameterise the melting that is driven by oceanographic processes associated with the ice-shelf cavities. The simulations should be regarded as an idealised test case of melting in the Amundsen Sea, not a fully realistic simulation of the real world.

https://doi.org/10.5194/egusphere-2026-2835
Preprint. Discussion started: 2 June 2026

2.2 Melting parameterisations

2.2.1 Overview

We follow previous authors in using our ocean model as an artificial 'ground truth' against which to test parameterisations of melting (Favier et al., 2019; Burgard et al., 2022; Burgard et al., 2023). However, there are a wide array of different parameterisations in the literature and it is impossible to test all of them. Our selection of which to test is guided by the following choices. First, our parameterisations may only use quantities available to a stand-alone ice sheet model (e.g. ice draft, far-field temperature). Second, we only test parameterisations that have a clear underpinning in the relevant physical theory, so that their behaviour can be clearly analysed and they may be expected to have wider applicability beyond the envelope of present-day conditions. Finally, we choose to only consider parameterisations that are *fully local*, in the sense that the melt rate at any location only depends upon quantities that are immediately relatable to that location, rather than requiring any prescription of an ocean circulation flow path. One motivation for this latter choice is that the sub-ice shelf flow fields are not straightforward, such that simply capturing the lateral transfer of information is a significant challenge that we defer for future studies. This choice also fits the general philosophy that we want to test the simplest and cheapest of formulations. Once we have established the abilities and shortcomings of very simple local formulations, we can consider the benefits of the more advanced parameterisations. The simulation output is available for anyone to test further parameterisations and we certainly welcome this. In the remainder of this sub-section we formulate a set of candidate melting parameterisations, and outline our approach to testing these against the model results.

2.2.2 Melting

The most widely-used formulation of ice shelf melting is the following set of equations, which is used in the model. These four equations express that the fluxes of momentum, heat, and salt must be conserved at the ice/ocean interface, and that the interface must remain at the pressure freezing point:

$$u_* = \sqrt{c_d}|\boldsymbol{u}| \tag{1}$$

$$\rho_i L_i m = \rho_o c_o \varphi \Gamma_T u_* (T - T_b) + \rho_i c_i m (T_i - T_b) \tag{2}$$

$$\rho_i m S_b = \rho_o \varphi \Gamma_S u_* (S - S_b) \tag{3}$$

$$T_b = \lambda_1 S_b + \lambda_2 + \lambda_3 P_b \tag{4}$$

Here, m is the melt rate; u_* is the friction velocity; T, S and $|\boldsymbol{u}|$ are the temperature, salinity, and current speed at the outer edge of the ocean boundary layer; T_b, S_b, and P_b are the interfacial temperature, salinity, and pressure; T_i is an internal ice shelf temperature, and all other physical constants and tuning parameters are listed in Table 1. While the applicability of this formulation to highly stratified areas in the Amundsen Sea remains under investigation (Vreugdenhil and Taylor, 2019; Davis et al., 2023; Rosevear et al., 2025), the model uses this formulation and it makes a logical starting point if we seek to parameterise the model results.

We note the presence of a novel factor φ in (2) and (3), which is a 'melting multiplier' introduced to clarify the issue of parameter tuning, which is widely used to calibrate the formulation (1)—(4). In previous studies, this parameterisation has been tuned in different ways, either through varying the drag coefficient c_d, or the heat and salt transfer coefficients Γ_T and Γ_S, or both. Such approaches can be problematic because the relative values of these three quantities reflect the molecular diffusivities of momentum, heat, and salt, which should not vary in principle. Also, the ice—ocean stress (1) is not only used in the melting parameterisation, but also as a boundary condition on momentum throughout the model and in the theoretical considerations below, so tuning c_d has a range of effects beyond melting. Therefore, in order to clarify that we are tuning melting only, we introduce φ. With the values adopted (Table 1), we are using $c_d = 0.0025$ in the momentum solve of the model, and matching the parameter values of Jenkins et al. (2010) in the melting formulation (i.e. equivalent to using a drag coefficient of 0.0097 in melting only).

Equation (2) expresses that heat is conserved; the latent heat consumption of melting (left-hand side) equals the convergence between the turbulent ocean heat flux towards the ice—ocean interface (first term on the right-hand side) and the conductive heat flux into the ice (second term). If we group the latent heat and conductive terms together, we arrive at a top-level expression for melting, which underpins all parameterisations that follow

$$m = \frac{\rho_o c_o \Gamma_T \varphi}{\rho_i L_i^*} u_* (T - T_b) \tag{5}$$

Where $L_i^* = L_i + c_i(T_b - T_i)$ can be treated as constant to a very good level of approximation (Jenkins, 2016). This leads us to expect that melting should be parameterised as the product of friction velocity u_* (linearly related to sub-ice current speed, according to (1)) and thermal driving $T - T_b$, the local temperature above the freezing point at the interface. In the below subsections we separately consider how to parameterise each of these two factors.

2.2.3 Thermal driving

Parameterising the thermal driving $T - T_b$ requires consideration of how oceanic heat reaches the ice shelves, and we proceed by considering the simplest approach available (Jenkins et al., 2018). We first replace the interfacial freezing point (T_b), which is calculated from the interfacial salinity (S_b) in (4), with the far-field freezing point (T_f) evaluated using the salinity at the edge of the boundary layer (S). As discussed by Jenkins et al. (2010), this amounts to neglecting the variation in turbulent salt fluxes through the ice—ocean boundary layer. However, the mean effect of salt mixing can be accounted for by re-defining the heat transfer coefficient, yielding:

$$\Gamma_T (T - T_b) = \Gamma_{\{TS\}} (T - T_f) \tag{6}$$

$$T_f = \lambda_1 S + \lambda_2 + \lambda_3 P_b \tag{7}$$

This provides an expression for the thermal driving as a function of temperature and salinity at the edge of the boundary layer and the pressure at the ice base. $T - T_f$ is sometimes referred to as thermal forcing.

Now, we propose that the boundary layer sits within a meltwater layer that is itself situated between the ice base and some deeper 'ambient' layer. The thermal forcing of the meltwater layer, $T - T_f$, lies somewhere between the ambient ocean thermal forcing $\left(T - T_f\right)_a$ and the thermal forcing evaluated at the ice base, which is zero. This can be expressed as $\left(T - T_f\right) = \varepsilon\left(T - T_f\right)_a$, where the factor ε is set by the relative strengths of the mixing between the ice and the meltwater layer, and the mixing between the meltwater layer and the ambient ocean (Jenkins et al., 2018). This mixing ratio ε is in reality a complicated function of the turbulent mixing in the meltwater current, but for simplicity it will be treated here as a constant, which is consistent with the use of constant mixing coefficients in the model simulations. Again following the simplest approach available, we now parameterise the 'ambient' temperatures and salinities at each location (T_a, S_a) as equalling the restoring ocean boundary condition profiles evaluated at the depth of the ice base (T^r, S^r), so that $\left(T - T_f\right)_a = \left(T^r - T_f^r\right)$.

Putting this all together yields

$$(T - T_b) = \frac{\Gamma_{\{TS\}}}{\Gamma_T}\varepsilon\left(T^r - T_f^r\right) \tag{8}$$

$$T_f^r = \lambda_1 S^r + \lambda_2 + \lambda_3 P_b \tag{9}$$

As desired, these formulae provide the thermal driving required in (5) as a function of quantities available to a stand-alone ice sheet model. The only variable is the ice-shelf draft, which sets P_b and the depth at which the ocean boundary conditions are sampled. The assumption that ambient properties equal the far-field properties is perhaps noteworthy, as it may appear to conflict with previous studies that have proposed schemes to represent the blocking of Circumpolar Deep Water currents by seabed ridges (Jourdain et al., 2020; Finucane and Stewart, 2024; Nicola et al., 2025). In fact, such modification can be considered within this framework by simply re-interpreting the mixing ratio ε as representing the modification between the model boundaries and the meltwater layer, rather than between the ambient and the meltwater layer.

2.2.4 Friction velocity

We derive simple expressions for the current speed beneath the ice by following established depth-integrated meltwater plume and layer theories (Jenkins, 1991; Holland and Feltham, 2006). Consider a local coordinate system with (x, y) directions oriented up- and along- the local ice base slope respectively. Then, neglecting all advective and diffusive transports in the horizontal direction to obtain a local formulation, we may depth-integrate the Navier-Stokes equations over a meltwater layer to obtain momentum equations in the local up-slope and along-slope directions:

$$\frac{d(DU)}{dt} = D\left(\frac{\rho_a - \rho}{\rho_0}\right) g \sin\theta - c_d|\boldsymbol{u}|U + fDV \tag{10}$$

$$\frac{d(DV)}{dt} = -c_d|\boldsymbol{u}|V - fDU \tag{11}$$

where D, U, and V are the layer thickness and up- and along-slope velocity components, ρ and ρ_a are the densities of the meltwater layer and ambient layer below, θ is the slope of the ice base, $|\boldsymbol{u}| = \sqrt{U^2 + V^2}$, and all other symbols are constants

https://doi.org/10.5194/egusphere-2026-2835
Preprint. Discussion started: 2 June 2026

and parameters listed in Table 1. The buoyancy force (first term on the right-hand side of (10)) is expressed according to Jenkins (1991), while the drag and Coriolis terms (remaining terms on the right-hand sides of (10) and (11)) are expressed according to Holland and Feltham (2006). From now on, we consider steady conditions, so the left-hand sides of (10) and (11) are set to zero and the terms on the right-hand sides have to balance each other.

The flow is driven solely by buoyancy in this formulation, so we consider limiting cases of whether drag or rotation balance the buoyancy force. Defining a characteristic velocity scale $\widehat{U} \sim \{U, V, |\boldsymbol{u}|\}$, the dimensionless ratio between the last two terms on the right-hand sides of (10) and (11) is $R = c_d \widehat{U}/|f|D$, with $R > 1$ implying drag is larger. This can be re-cast as implying a critical time scale, such that drag dominates if $D/\widehat{U} < c_d/|f|$. With the parameters used here, $c_d/|f| \sim 18$ s (Table 1), so for a 10 cm/s flow, a meltwater layer shallower than 1.8 m will experience a greater drag force than Coriolis force. Crucially, R shows that shallower, faster meltwater layers will be dominated by a balance between buoyancy and drag forces, while deeper, slower layers will be dominated by a balance between buoyancy and Coriolis forces.

Taking the limiting case where $R \gg 1$ and neglecting the Coriolis term in (10) and (11) altogether, the cross-slope velocity is zero and the flow is purely up-slope, in a 'terminal velocity' balance between buoyancy and drag:

$$D\left(\frac{\rho_a - \rho}{\rho_0}\right) g \sin\theta = c_d U^2, \quad V = 0 \tag{12}$$

Taking the opposite extreme of $R \ll 1$ and neglecting the drag term in (10) and (11) altogether, the up-slope velocity is zero and the flow is purely along-slope, in a geostrophic balance between buoyancy and rotation:

$$D\left(\frac{\rho_a - \rho}{\rho_0}\right) g \sin\theta = -DfV, \quad U = 0 \tag{13}$$

Utilising (1), these arguments yield two limiting cases for the friction velocity:

$$u_* = \begin{cases} \left(\dfrac{g}{\rho_0} D(\rho_a - \rho) \sin\theta\right)^{\frac{1}{2}} & R \gg 1 \quad \text{buoyancy} \sim \text{drag} \quad (14) \\ \dfrac{\sqrt{c_d}\, g}{f \rho_0} (\rho_a - \rho) \sin\theta & R \ll 1 \quad \text{buoyancy} \sim \text{rotation} \quad (15) \end{cases}$$

We test the applicability of these simple dynamical theories below. However, u_* is not yet closed because we need an expression for the meltwater layer density anomaly relative to the ambient $(\rho_a - \rho)$. With a linear equation of state and equal mixing of heat and salt, the temperature, salinity, and density anomalies caused by melting ice are all linearly related (Jenkins, 2016). Therefore, the density anomaly of the meltwater layer relative to the ambient ocean scales linearly with the analogous temperature anomaly, $(\rho_a - \rho) = P_0(T_a - T)$, where the factor P_0 defined in Jenkins et al. (2018) is approximately constant over the range of temperatures and salinities beneath Amundsen Sea ice shelves. As described in the preceding section, we may assume that the temperature of the meltwater layer, T, lies somewhere on a mixing line between the ambient ocean temperature (T_a) and the freezing point (T_b), so $(T - T_b) = \varepsilon(T_a - T_b)$. Combining these concepts yields an expression for the density anomaly as a function of the thermal driving

$$(\rho_a - \rho) = P_0\left(\frac{1-\varepsilon}{\varepsilon}\right)(T - T_b). \tag{16}$$

Inserting (16) into (14) and (15), we may then parameterise the friction velocity as a function of the thermal driving (8).

2.2.5 Melting near the grounding line

One area where the above theories may break down is in the thin sub-ice cavities near grounding lines, for which very few observations exist (e.g. Minowa et al., 2021; Schmidt et al., 2023). The physics of these regions is still an active area of research and a comprehensive physical description is yet to emerge. Subglacial outflows are thought to have an important influence on ocean buoyancy and the mixing of heat (Jenkins, 2011; Le Brocq et al., 2013; Horgan et al., 2025), and tides are expected to lead to strong mixing (Holland, 2008; Begeman et al., 2018; Rignot et al., 2024), but the model neglects both subglacial outflows and tides. Without these effects, we may expect ocean currents to decrease to zero at the static grounding line, and (5) implies that melting also decreases to zero. This result also arises from the dynamical theory in section 2.2.4: As the meltwater layer thins, drag terms become proportionately more important, the ratio R becomes large, (14) describes the meltwater flow, and $u_* {\sim} D^{1/2}$ decreases to zero. As a result, we expect the friction velocity and melt rate to decrease to zero as the grounding line is approached.

It is not clear what functional form this decrease in melting might follow, since the thermal driving and buoyancy anomaly are also expected to decrease towards the grounding line (e.g. Minowa et al., 2021; Schmidt et al., 2023), owing to enhanced mixing in the thinner water column and a reduced supply of heat and salt by the weakening mean circulation. It is also not clear how the melting will vary with the declining friction velocity, since double-diffusive processes and molecular diffusion may grow in importance as the mean currents reduce (Rosevear et al., 2025). Here, we take the simplest approach and test the impact of simply tapering parameterised melting linearly to zero at the grounding line over a specified length scale. This is implemented by introducing a tapering function that has a value of 1 over most of the ice shelf area but decreases to zero as each ice shelf grid cell point $\boldsymbol{x}$ approaches its closest grounded ice grid cell point $\boldsymbol{x}_{\boldsymbol{g}}$ over the length scale δx

$$\Psi(\delta x) = \min\left(\frac{|x - x_g|}{\delta x}, 1\right) \tag{17}$$

2.2.6 Resultant parameterisations

Combining expressions for melting (5), thermal driving (8) and (9), friction velocity (14) and (15), buoyancy (16), and tapering (17), we arrive at

$$m = \begin{cases} \left[\dfrac{c_o \varphi \Gamma_{\{TS\}}}{\rho_i L_i^*}^{3/2} \left(\dfrac{\rho_o g P_0}{\Gamma_T} \varepsilon^2 (1-\varepsilon) D \right)^{1/2} \right] \left(T^r - T_f^r \right)^{3/2} (\sin\theta)^{1/2}\, \Psi(\delta x) & R \gg 1 \quad \text{buoyancy} \sim \text{drag} \qquad (18) \\ \left[\dfrac{c_o \varphi \sqrt{c_d}\, g \Gamma_{\{TS\}}{}^2 P_0}{\rho_i L_i^* f \Gamma_T} \varepsilon (1-\varepsilon) \right] \left(T^r - T_f^r \right)^2 (\sin\theta)\, \Psi(\delta x) & R \ll 1 \quad \text{buoyancy} \sim \text{rotation} \quad (19) \end{cases}$$

From now on, we regard the quantities in the square brackets as constant, yielding local parameterisations of melting in terms of temperature above freezing (from ocean boundary conditions), ice base slope, and distance to grounding line, all quantities available to an ice sheet model. The factors in the square brackets have been discussed at length by Jenkins et al. (2018) and references therein, and most of these should be constant. The greatest uncertainty lies in the mixing ratio ε and layer thickness D, which are controlled by turbulent mixing in the meltwater layer, which remains an active area of research (Vreugdenhil and Taylor, 2019; Davis et al., 2023; Anselin et al., 2024; Davis et al., 2025; Rosevear et al., 2025). In order to make progress with a simple parameterisation we treat these quantities as constant, and each of the square brackets in (18) and (19) is treated as a single tuning parameter.

Before proceeding, we note that (18) and (19) are representative of many formulations that have previously appeared in the literature. Based on local geostrophic theory, the quadratic dependence on temperature in (19) was first proposed by Holland et al. (2008), and its linear slope dependence identified by Jenkins et al. (2018), with both dependencies verified theoretically by Jenkins (2021b). MacAyeal (1984) had previously proposed a local quadratic law, but this was derived by balancing buoyancy with tidal drag, rather than Coriolis force, and is ill-posed in the absence of tides. If we replace the tidal drag with meltwater drag, the derivation of MacAyeal (1984) yields an expression nearly identical to (18), with temperature to the 3/2 power and slope to the 1/2 power. In the absence of rotation, Jenkins (2021a) describes how simple one-dimensional line plume theory leads to (18). Lazeroms et al. (2018) examine the buoyancy~drag formulation that leads to (18). In a local formulation of the problem, they find the same dependence on temperature to the 3/2 power and layer thickness to the 1/2 power, though their slope dependence differs from (18) because they assume that turbulent mixing varies with slope. More importantly they, and many subsequent authors, focus on a nonlocal formulation whereby the layer thickness D scales with temperature, which then yields a quadratic dependence on temperature overall (see (18)) (Lazeroms et al., 2018; Favier et al., 2019; Lazeroms et al., 2019; Burgard et al., 2022). In summary, the power-law dependence of melting on temperature and ice base slope remains uncertain, as a result of uncertainty in whether buoyancy is balanced by Coriolis force or drag, in the controls over turbulent mixing, and whether the meltwater can be reasonably represented as being in a local balance.

2.2.8 Parameterisation calibration and assessment

Following the above discussion, we focus our parameterisation testing on the following structure:

$$m = C\left(T^r - T_f^r \right)^{\alpha} (\sin\theta)^{\beta}\, \Psi(\delta x) \qquad (20)$$

where $\alpha \in \{1, {}^{3}/_{2}, 2\}$, $\beta \in \{0, {}^{1}/_{2}, 1\}$, δx is varied between 0 and 5 km, and the coefficient C is calibrated separately for the parameterisation structure arising from each choice. We only test (α, β) combinations that have some basis in physical theory. The calibration procedure is as follows. For each combination of $(\alpha, \beta, \delta x)$ we calculate the melt rate field arising from the resulting parameterisation, using boundary restoring temperatures, ice slopes and grounding line from the reference present-day simulation. Then, we compare this to the melt field predicted by the model in that simulation. The value of C for each parameterisation structure is selected using ordinary least-squares linear regression to minimise misfit between the parameterised and modelled melt fields over all ice shelves Dotson—PIG. We emphasise that this regression has no intercept, i.e. the value of C is chosen assuming that melting is zero when the right-hand side of (20) is zero. For comparison later in the paper, we also test setting melting equal to a tuned linear function of ice draft z_b, again with no intercept to avoid predicting freezing at shallower depths.

The assessment procedure for each parameterisation is as follows. After calibration, we first assess the coefficient of determination (r^2) between the parameterised and modelled melt rate fields for the reference present-day simulation, which is the quantity minimised in the calibration. We interpret this as quantifying what fraction of the spatial melt rate pattern variance the parameterisation structure is able to capture, after tuning. We select this metric because it is sensitive to both the rate and the location of melting, which are both important to glacier dynamics (Morlighem et al., 2021; Naughten et al., 2023). We note that this does not equal the square of the Pearson correlation coefficient because (20) has no intercept. Next, we apply the same parameterisations to the retreated future ice geometries, and compute the r^2 between parameterised and modelled melting fields, without recalibrating the coefficients C. We interpret this as quantifying what fraction of the future melt field spatial variance the parameterisation is able to predict, based only on present-day information. We also assess the Mean Absolute Error for each parameterisation.

3 Results

3.1 Modelled melting in present day

Figs. 1a and 1b show the model domain, seabed, and ice draft geometry. We only model the south-easternmost sector of the Amundsen Sea shelf, in order to obtain the best possible resolution of cavity circulation and melting beneath PIG, Thwaites, and Dotson—Crosson ice shelves, which are the key regions of ocean-induced glacier change (Rignot et al., 2019; Shepherd et al., 2019; Selley et al., 2025). These ice-shelf cavities are linked to the shelf break by the Pine Island—Thwaites Trough and the Dotson Trough (Fig. 1a). Fig. 1c maps the maximum ocean temperature at any depth in the water column in the reference present-day simulation, showing how warm and saline Circumpolar Deep Water floods these troughs, connecting the warm deep Southern Ocean directly to the ice shelf cavities. There is a cooling within the cavities of PIG and Crosson ice

https://doi.org/10.5194/egusphere-2026-2835
Preprint. Discussion started: 2 June 2026

shelves but, broadly speaking, Circumpolar Deep Water is able to access the deepest areas of the ice base throughout the sector.

Fig. 2 shows a closer view of the ice draft, melt rates, and sub-ice shelf currents for the three main ice shelves in the eastern Amundsen Sea. The velocity vectors shown are the mean horizontal currents over the top 10 m of the model grid under the ice shelves, as used in the melting formulation according to the boundary-layer scheme of Losch (2008), and for clarity each plotted vector represents the mean of an 8×8 square of model grid cells, illustrating the high model resolution used in this study. This figure shows two clear features that dominate the melting pattern. First, there are 'hot spots' of high melting above 100 m/y in the four thick ice inflows at PIG trunk, Thwaites Inlet, Smith Inlet, and Kohler Inlet. The extremely high melt rates in these hot spots arise because the deep ice base is sitting in the warm Circumpolar Deep Water layer, and hence has strong thermal forcing, and is also steeply sloping, and hence has strong buoyancy-driven meltwater currents. Second, each of these hot spots serves as a source for 'meltwater outflows', which travel up and across the base of the ice. These out-flowing currents are guided by a balance between up-slope buoyancy force, across-current Coriolis force, and against-current drag forces, and predominantly travel along ice draft contours, with thicker or grounded ice to their left (Holland and Feltham, 2006). We now consider each of these ice shelves in turn, focussing solely on the ocean processes directly controlling melt patterns.

For PIG, a detailed understanding of melt rate patterns has been gained from remote sensing studies (Dutrieux et al., 2013; Shean et al., 2019; Lowery et al., 2025). These patterns are dominated by very high melt rates exceeding 100 m/y over a substantial portion of the thick ice in the main PIG trunk. This high melting is extremely heterogeneous, with melting varying between hundreds of metres per year and near-zero in response to kilometre-scale channels and undulations in the ice base. The model reproduces the high, heterogeneous melting in this area (Fig. 2d), though we do not expect the detail of the channelised melt patterns to be accurate given the model resolution of 400 m. Satellite-derived melt rates are lower over most of the remaining ice shelf, below 20 m/y, but with a noticeable increase in the northern half of the main ice outflow (Shean et al., 2019; Lowery et al., 2025), which the model reveals to be driven by a relatively fast-moving meltwater outflow (Fig 2d). An apparently lesser outflow also emerges on the southern shear margin. The existence of both of these outflows is supported by oceanographic observations along the ice front (Dutrieux et al., 2014; Naveira Garabato et al., 2017) and the formation of polynyas at the sea surface (Payne et al., 2007; Mankoff et al., 2012; Savidge et al., 2023), but these observations show that the southern outflow is much stronger. Two-dimensional meltwater layer models predict that this southern outflow supports higher melt rates (Payne et al., 2007; Lambert et al., 2023), but three-dimensional cavity models agree with satellite-derived melt rates that the northern outflow drives melting that is stronger or comparable (Dutrieux et al., 2014; Nakayama et al., 2019; Nakayama et al., 2021; Lowery et al., submitted). Lowery et al. (submitted) explain this situation by showing that the stronger southern outflow is largely separated from the ice base by a fresher, colder layer of meltwater that 'pools' beneath the southern shear margin of PIG. Since the meltwater outflow is separated from the ice base it cannot drive stronger melting.

For Thwaites ice shelf, mapping melt rates from satellite observations is much more challenging, because the most rapidly melting areas near the grounding line are heavily damaged and not a continuum, and often held out of floatation by ice bridging stresses. However, the available data (Milillo et al., 2019; Chartrand et al., 2024; Gourmelen et al., 2025) clearly demonstrate that strong melt rates of over 100 m/y are present near the rapid inflow of ice through Thwaites main trunk, in Thwaites Inlet. Much weaker melt rates of only a few metres per year are derived on the larger eastern ice shelf, which is supported by direct field observations (Davis et al., 2023; Schmidt et al., 2023; Wild et al., 2024; Davis et al., 2025), and the much lower ice influx/ divergence in this sector. High-resolution ocean models capture this pattern, with a melting 'hot spot' in Thwaites Inlet (Nakayama et al., 2019; Holland et al., 2023), as also found here (Fig. 2e). The remaining intact ice shelf in Thwaites Inlet is only about 10 km long, with the remainder of Thwaites' western ice tongue consisting of a mass of calved icebergs and melange (Fig. 2b; Miles et al., 2020; Bevan et al., 2021). This means that the meltwater outflow attached to the ice base is much shorter than in other areas, and basically confined to the hot spot region (Holland et al., 2023). This current heads north under the influence of Coriolis force, along the ice draft contours, because the background ice draft gradient in Thwaites Inlet is west-to-east. Some observational support for this outflow is provided by polynyas that open within the melange immediately to the north, though apparently only in times of high subglacial outflow from beneath Thwaites Glacier (Gourmelen et al., 2025), which is not modelled here.

For Dotson—Crosson Ice Shelf, satellite-derived melting studies have focussed on the meltwater outflow beneath Dotson Ice Shelf (Gourmelen et al., 2017; Zinck et al., 2023), which is also clearly observed in oceanographic observations across the Dotson ice front (Jenkins et al., 2018) and reproduced by our model (Fig. 2f). Goldberg et al. (2019) extend the coverage of satellite-derived melting maps, finding high melt rates in the region where Dotson and Crosson ice shelves join, and the suggestion of a meltwater outflow on the northern edge of Crosson Ice Shelf, next to Bear Island, both of which are also modelled here. All of these studies show very high melt rates in Kohler Inlet, in agreement with the modelled hot spot in that location, though none of the satellite datasets cover the Smith Inlet hot spot. Previous modelling studies produce qualitatively similar results to those found here (Goldberg et al., 2019; Lambert et al., 2023; Shrestha et al., 2024).

These results provide a detailed examination of ice shelf melting across these four cavities, and a suitable test-bed for our primary aim of testing melting parameterisations. Nevertheless, there are a few caveats that should be noted: we neglect the influence of subglacial outflows into the ocean, though it can have a local effect on melting near grounding lines (Nakayama et al., 2021; Gourmelen et al., 2025). We only consider the time-mean melt rates, neglecting the influence of turbulent eddies (Shrestha et al., 2024; Poinelli et al., 2025), seasonal variability (Davis et al., 2018; Mallett et al., 2018), and interannual to decadal variability (Dutrieux et al., 2014; Jenkins et al., 2018). Finally, as described in section 2.1.3 above, the waters in

Dotson Trough should in reality be cooler than those in Pine Island—Thwaites Trough (Jacobs et al., 2012), but we neglect this difference in order to clarify the testing of parameterisations.

3.2 Evaluation of best-performing parameterisation

We now consider how well the local melting parameterisations derived in section 2.2 are able to reproduce the melting fields from the model. Before proceeding, it is important to clarify the length scales under consideration in this study. Our primary aim is to parameterise the ice shelf melting patterns that are important to ice-shelf buttressing. However, modelled ice-shelf melting varies substantially down to the smallest scales due to the presence of channels, crevasses, and other features in the ice shelf bases (Fig. 2). With a grid resolution of 400 m we do not resolve these features, and in any case they are unlikely to affect ice shelf buttressing on a glacier-wide scale, or at least it is only their averaged effect on melting that affects buttressing. Therefore, in the parameterisation evaluation we smooth all fields by replacing each grid cell value with a box-average of all values within a radius of 3 cells, i.e. a 7×7 box (2.8×2.8 km). This smoothing is applied to both the target melt rates (Figs. 3a-c) and all of the fields entering the parameterisations.

Table 2 shows the metrics assessing a range of different parameterisation structures against the melt rates from the full model, according to the pattern correlation (coefficient of determination) between modelled and parameterised melt rate fields, and the mean absolute error. Given the extreme simplicity of these local parameterisations the metrics are perhaps surprisingly favourable, with pattern correlations of r^2~0.6 and mean error of ~6 m/y for most of the formulations considered. We interpret these r^2 values as demonstrating that the parameterisations are able to capture 60% of the spatial variance of the melting pattern in the full model. The best-performing parameterisation is found to be expression (18), on the first line of Table 2, with r^2=0.649. We now focus on illustrating the characteristics of this parameterisation, with the other parameterisations compared below in section 3.4.

Figs. 3a-c show the smoothed model melt rates, which mostly removes the high-spatial-frequency features to leave the melting patterns associated with near-grounding-line hot spots and Coriolis-influenced meltwater outflows. Figs. 3d-f show the results of expression (18), when fed with the smoothed ice-base slopes and ocean boundary temperatures and freezing temperatures projected horizontally onto the ice base draft, and tapered to zero over 3 km near the grounding line. Like all parameterisations, the constant multiplying this expression, C = 40.3, has been tuned to maximise the fit. It is immediately apparent that this parameterisation broadly captures the four hot spots of high melting in general near the grounding lines, though it does not capture the detailed patterns of melting within those hot spots. It also has no way of representing the Coriolis-influenced outflows, e.g. beneath PIG and Dotson ice shelves. However, this general ability of being able to capture localised high melt rates in excess of 100 m/y near the deep grounding line, while producing much lower melting over the remainder of the ice shelf, is encouraging for the possibility of using this parameterisation to drive an ice-sheet model.

https://doi.org/10.5194/egusphere-2026-2835
Preprint. Discussion started: 2 June 2026

Fig. 4 investigates the modelled and parameterised processes controlling PIG melting. The top row illustrates the model results, with the melting (Fig. 4a) being proportional to the thermal driving (Fig. 4b) multiplied by the sub-ice ocean current speed $|\boldsymbol{u}|$ (Fig. 4c), according to (5) and (1). From these figures we can see that the melting hot spot occurs because the deep trunk of PIG is both sitting in warm waters and hosts very rapid sub-ice currents, as a result of the steep ice-base slope and strong production of buoyant meltwater. It is also apparent that the higher melting on the northern side of the main trunk is supported by the high flow speed of the Coriolis-influenced outflow, not by anomalously warm waters in this region.

The bottom row of Figure 4 illustrates the parameterised analogue of these three quantities, as implied by the structure of (18). The melting (Fig. 4d) is exactly as shown in Fig. 3. The parameterised thermal driving (Fig. 4e) is derived from the restoring boundary temperature (T^r) and the freezing temperature derived from the restoring boundary salinity (T_f^r), evaluated at the ice-base depth in each location, as in (8) and (9). The field plotted in Fig. 4e is the result of optimally scaling $(T^r - T_f^r)$ to match the modelled thermal driving over all ice shelves. The match to the modelled thermal driving is very good, with a pattern correlation of r^2=0.786 across all ice shelves. This is perhaps unsurprising, because the thermal structure of the Amundsen Sea is relatively simple, with temperatures increasing with depth. However, this result should not be taken to mean that the deep waters on the shelf simply contact the ice base without modification. The coefficient of best fit between the modelled thermal driving and $(T^r - T_f^r)$ is 0.502, so the thermal driving at the ice base is half that implied by the boundary conditions. This is because the warmest waters are prevented from contacting the ice base by mixing with cooler waters over the shelf, the presence of seabed sills within the cavities (Fig. 1c), and the cooler meltwater layer beneath the ice.

The parameterised friction velocity (Fig. 4f) is a different story. The parameterised current speed plotted here, $\left(T^r - T_f^r\right)^{1/2} (\sin\theta)^{1/2}\, \Psi(3\text{ km})$, is derived by assuming that meltwater flow arises from a buoyancy—drag balance (14) where the buoyancy scales with the thermal driving (16) and the velocity decays to zero toward the grounding line (17). Again, this quantity is optimally scaled to match the modelled friction velocity. This is the most skilful parameterisation for meltwater flow speed that we have tested, but the fit is still extremely poor, with r^2=0.139. The parameterisation captures the basic existence of rapid buoyancy-driven meltwater flows within the melting hot spot. The success of this particular formulation within the hot spot makes some sense because the buoyancy—drag balance is most appropriate in this region of thin, fast-flowing meltwater (see section 2.2.4). However, the parameterisation is clearly unable to capture the detailed pattern of the rapid flows within this region, nor does it have any structural capacity to capture the Coriolis-influenced meltwater currents. For these reasons, the parameterised and modelled current speeds are basically uncorrelated, and this means that the parameterised melt rate performs less well than the parameterised thermal driving. Clearly, obtaining better

https://doi.org/10.5194/egusphere-2026-2835
Preprint. Discussion started: 2 June 2026

parameterisations of sub-ice current speeds is the route to unlocking the remainder of the predictive skill that is absent from the formulation (18).

3.3 Performance using future geometries

The primary usage case that we envisage for an ice-shelf melting parametrisation is to produce ice-sheet forecasts cheaply, without the need for a coupled ocean model. In that regard, it is useful to consider the parameterisation skill under future ice-sheet conditions. To this aim, we also perform high-resolution ocean model simulations for five future ice sheet geometry time slices derived from a coupled ice/ocean simulation of Bett et al. (2024). Figs. 5a-c shows the present-day geometry considered previously and also two snap shots of modelled ice shelf geometry after 108 and 180 years of the coupled ice/ocean simulation, which uses an idealised warm ocean forcing scenario. The ice thins rapidly in response to the warm scenario in these coupled simulations, causing substantial grounding-line retreat and leading to large ice shelves because the ice front is held fixed (Bett et al., 2024). Dotson—Crosson Ice Shelf thins over most of its area, with just a few thick inflowing glaciers remaining, PIG retains a thick central trunk, and Thwaites becomes a huge ice shelf due to its substantial grounding-line retreat, with steep slopes near the grounding line and sloping more gently towards the ice front. The characteristics of this large future Thwaites ice shelf are governed by the existence of pinning points that form and unground during the retreat (Bett et al., 2024).

Figs. 5d-f show the modelled melt rates for these ice geometries, using the same representation of present-day average forcing as the previous simulation. It is clear that high melt rates follow the deep ice as the grounding-line retreats. PIG and Doston—Crosson melting hot spots stay qualitatively the same, while the small melting hot spot in Thwaites Inlet develops into a wide strip of melting along the grounding line, maintaining rapid melting over a rapidly expanding area of deep ice as the Thwaites sector deglaciates. Figs. 5g-i show the result of applying the parameterisation (18), tuned in the present-day, to the time-varying ice geometries, clearly capturing the same pattern as the full ocean model, albeit with slightly less intense peak melt rates near the grounding line.

Fig. 6 quantifies the evolution of area-integrated melting over the five future time slices of ice geometry, for both the high-resolution ocean model results and the parameterisation (18). The simple parameterisation fails to capture a rapid modelled doubling in PIG melting, which later dies away (Fig. 6c), but quite accurately captures the smaller changes in Dotson—Crosson Ice Shelf (Fig. 6d). Importantly, however, the parameterisation accurately reproduces the very strong melting feedback in Thwaites Glacier (Fig. 6b). This is because the feedback is relatively simple; as demonstrated by Bett et al. (2024), the total melting flux increases in proportion to the area of deep ice shelf base sitting in warm Circumpolar Deep Water, which increases rapidly as the grounding line region widens and retreats into a deeper bed. The high melt rates are reproduced in the parameterisation because deeper ice sits in the warmer deep water in the boundary conditions, hence a

https://doi.org/10.5194/egusphere-2026-2835
Preprint. Discussion started: 2 June 2026

higher value of $\left(T^r - T_f^r\right)^{3/2}$, and also has a steeper slope, hence a higher $(\sin\theta)^{1/2}$. Since the future increase in Thwaites melting is so large, it dominates the changes in other ice shelves, and so the parameterisation performs reasonably well in capturing the increase in meltwater flux over the whole sector (Fig. 6a).

3.4 Performance of other formulations

The theoretical considerations of section 2.2 could support different parameterisation formulations, and we saw in Table 2 that several of these perform reasonably well when compared with the model. This comparison is further illustrated and extended to future ice geometries in Fig. 7. Fig. 7a shows the integrated melt flux over all ice shelves for the model and a range of different parameterisations, analogous to Fig. 6a. Fig. 7b shows the pattern correlation between the modelled and parameterised melt rate fields for each parameterisation, for each time slice. Taken together, Table 2 and Fig. 7 show two best-performing parameterisations: The formulation (18) considered so far (red lines in Fig. 7), and a quadratic dependence upon thermal driving with no slope dependence (blue lines in Fig. 7). The pattern correlation of each of these in the present day is improved by adopting a tapering to zero towards the grounding line (Table 2), but this tapering seems to have little benefit over future geometries (green lines in Fig. 7). The simple quadratic formulation has been widely used in previous literature (e.g. Holland et al., 2008; Jourdain et al., 2020) and seems to perform slightly better in future projections (Fig 7a). However, its physical underpinning is less clear, since an additional linear slope dependence is implied in (19), and including this slope dependence degrades both the pattern correlation and quantitative melt rates (cyan lines in Fig. 7). A simple parameterisation of melting as a function of depth performs poorly in terms of pattern correlation (pink lines in Fig. 7).

In summary, we favour the parameterisation (18) because it best matches the modelled melt pattern in the present day geometry, performs relatively well with future geometries, and has a clear theoretical underpinning. However, in terms of parameterisation skill alone, comparable results are found by neglecting the taper to zero near grounding lines, or simply adopting the commonly-used quadratic formulation. All parameterisations tested reproduce the strong feedback of future ice geometric change onto melting (Fig. 7a), attesting to the simplicity of this feedback, with ice melting enhanced as the Thwaites grounding line creates a larger area of ice in deep warm water (Bett et al., 2024).

4 Discussion

This study seeks to make progress in two areas: Enhanced understanding of ice-shelf melting in the Amundsen Sea and the ability of simple local parameterisations to capture it. The focus is on projections of ice loss from this sector, so we avoid detailed consideration of wider oceanographic processes in the Amundsen Sea, or any consideration of other sectors.

4.1 New insights into melting of Amundsen Sea ice shelves

The high-resolution ocean model results produce new insight into the processes supporting melting of Amundsen Sea ice shelves. Fig. 8 shows modelled melt rates and sub-ice currents, as in Fig. 2, but with two additional contours, enclosing ice-shelf area that accounts for 50% and 90% of the total basal melting mass flux from this sector. These contours are calculated by sorting the grid-cell melt rates from high to low, calculating a running total for each grid cell, and dividing that field by the total basal mass loss from the sector. The results highlight the four 'hot spots' of melting beneath the deep glacier inflows (PIG trunk, Thwaites Inlet, Smith Inlet, Kohler Inlet), which all have melt rates in excess of 100 m/y and between them account for 50% of the total basal mass flux. These hot spots exist because the ice is bathed in deep warm waters, and is steeply sloping, producing vigorous meltwater flow that supports a high turbulent heat flux towards the ice.

Also apparent in Fig. 8 are the 'meltwater outflows' emanating from these hot spots, particularly noticeable in northern PIG and western Dotson Ice Shelf. Under a balance between buoyancy, Coriolis force, and drag, meltwater currents are predominantly directed along ice-draft contours, flowing with thick ice to their left (Holland and Feltham, 2006). This explains the northward flows beneath Thwaites Inlet and Dotson Ice shelf, which have thicker ice to their west (Fig. 2), and the north-westward flow beneath PIG, which has the thick trunk of the glacier to its south-west. The southern PIG outflow appears weaker, because the meltwater flow is detached from the ice base in this region (Lowery et al., submitted). The Crosson Ice Shelf outflow is also a relatively weak feature, and is trapped to its left by the grounded Bear Island, rather than thicker ice (Fig. 2). Between these two general features of 'hot spots' and 'meltwater outflows', we are able to account for 90% of the basal mass flux from the ice shelves in this sector (Fig. 8).

The total basal melting controls the mass balance of the ice shelf, but changes in ice-shelf mass can only influence the grounded ice sheet (hence sea-level rise) if they alter the flux of ice across the grounding line. Therefore we must also consider the ice-sheet momentum balance, and the extent to which floating ice resists grounded ice-sheet flow. This 'buttressing' force primarily arises through basal stresses on grounded ice-shelf pinning points, lateral stresses across ice-shelf shear margins, and resistance to laterally-convergent flow in concave grounding-line inlets. As a result, melting in these regions is disproportionately influential on grounded ice loss. Fig. 9 shows three independent quantifications of the sensitivity of grounded ice loss to changes in ice-shelf melting, derived through either large ensembles of ice model sensitivity experiments (Reese et al., 2018b; Naughten et al., 2023) or through an adjoint of the forward ice sheet model derived by algorithmic differentiation (Goldberg et al., 2019; Morlighem et al., 2021; Gourmelen et al., 2025). Buttressing can also be quantified directly by considering the ice stress regime along the grounding line (Gudmundsson et al., 2023).

While the three different fields are not always in agreement, Fig. 9 shows two broad classes of melt sensitivity that interface directly with the melting features described above. First, it is immediately apparent that PIG buttressing is dominated by its shear margins, and this is also the case for the northern shear margin of Crosson Ice Shelf. Meltwater outflows control melting of the ice base in all of these regions (Fig. 8), so that any change in these outflows would directly influence grounded ice loss. Second, there are regions of elevated melt sensitivity in smaller concave embayments in the grounding line, most notably in Kohler Inlet and Thwaites Inlet, such that any changes in the hot spots of very rapid melting found in these regions will be influential. It is important to note that the gridded fields in Fig. 8 may under-represent the sensitivity in near-grounding-line regions, both due to the coarse grids used and also because their methodology reflects only instantaneous ice velocity response to melting changes, neglecting feedbacks induced by grounding-line retreat. Analysis of the grounding-line stress regime also emphasises the high buttressing in individual bays along the grounding line, most notably in Thwaites Inlet but also for the other ice shelves (Gudmundsson et al., 2023). Also, Bett et al. (2024) highlight the importance of pinning points near grounding lines in controlling the future retreat of Thwaites Glacier. Thus, the melting hot spots and meltwater outflows identified above both melt ice shelves in regions that strongly influence grounded ice loss.

4.2 Assessment of simple local parameterisations

A range of simple, local parameterisations are tested for their ability to reproduce the modelled melt rates, using present and future geometries, with their skill quantified in Table 2 and Fig. 7. Our assessment is that the expression (18) offers the best performance, expressing melting as a function of temperature to the power 3/2, slope to the power 1/2, and tapered to zero near the grounding line. This assessment is based on the spatial pattern fit to modelled melt rates for both present-day and future geometries, the ability to capture the strong melting feedback beneath Thwaites Glacier, and the clear theoretical foundation of this formulation. Taken at face value, this result has several implications: 1) the sensitivity of melting to ocean warming is above linear; 2) there is a feedback onto melting as the grounding line retreats into deeper water, exposing more of the ice base to warm ocean forcing; 3) there is a feedback as melting steepens the ice base slope; 4) ice-shelf melting declines near grounding lines. However, there are two major restrictions in drawing these conclusions: Firstly, the model used to evaluate the parameterisations has its own limitations, and secondly a similar skill can be obtained by removing the taper, or employing the commonly-used quadratic function of temperature with no slope dependence (Holland et al., 2008; Jourdain et al., 2020). Thus, conclusions 1 and 2 are more robust than conclusions 3 and 4.

The tapering of melt rates to zero near grounding lines is subject to substantial uncertainty because even this high-resolution model cannot resolve processes in these thin ocean cavities. In addition, the bathymetry is poorly known, and the ice draft is uncertain because the ice is not freely floating. The dominant processes controlling the melting of ice shelves near grounding lines are not well-constrained by observations, and the resulting melt patterns represent an open research question that is beyond the scope of the present study. With these caveats noted, we find that tapering melt rates to zero near grounding lines always improves the parameterisation skill in capturing the modelled fields (Table 1).

The value of introducing ice-base slope into a melting parameterisation is not clear empirically, because the skill is approximately equal between the expression (18) and a quadratic temperature formulation with no slope dependence. While this basic quadratic formulation has been very widely used, our derivation of (19) implies it should have a linear slope dependence, but we find that formulation to be significantly less skilful. It is arguable whether this slope dependence should appear; for example, the mixing efficiency ε could be slope-dependent (Jenkins et al., 2018), which would influence the overall form of (19). The geophysical impact of including a slope in the melting parameterisation should also be borne in mind. In a coarser-resolution ice or ocean model the steepest slopes would reflect the large-scale thinning of thick inflowing ice trunks, but in our high-resolution simulations, the steepest slopes are on the flanks of subglacial channels (e.g. Figs. 3d-f), so it is possible the parameterisation usage case will differ from the evaluation performed here. Nevertheless, a dependence of melting on slope to the 1/2 power forms part of our best-fit parameterisation and is also supported by modelling of boundary-layer turbulence (Anselin et al., 2024).

The results of this study suggest that many parameterisation approaches should be able to represent the hot spots of melting if appropriately tuned, including simple functions, box models, and plume theory (Burgard et al., 2022). This implies that near-grounding-line buttressing sensitivities (Fig. 9) should be captured by these simple approaches, which is an extremely useful result. It seems far more challenging for parameterisations to represent the Coriolis-influenced meltwater outflows that control melting beneath buttressing shear margins, for which two-dimensional meltwater layer models or three-dimensional ocean models are probably required (Lambert et al., 2023). We note that all of our inferences are applicable only to the Amundsen Sea, where the parameterisation success is largely due to the simplicity of the ocean temperature structure; thick ice sits in warm, deep water, and hence melts more. The role of sills in reducing the access of this warm water to the ice base seems to be simply captured within the parameterisations, which may be because the warm deep layer is relatively uniform and the sills do not reach far into the thermocline. Previous studies have found that simple local formulations perform well in this region, but require adaptations (e.g. using nonlocal temperatures or slopes) when applied to all Antarctic ice shelves (Burgard et al., 2022; Burgard et al., 2023).

It is important to note that the highlighted parameterisations cannot be any more realistic than the model results used for tuning. No model is perfect and important structural differences remain between the results of different ocean models applied to sub-ice shelf flow (Yung et al., 2026). While the model resolution is very high (400 m horizontal by 10 m vertical), it is still not high enough to properly resolve sub—ice Ekman layers (Patmore et al., 2023) or the tapering of melt near grounding lines. The constant diffusivities and viscosities in the model could also be expected to impact the tuned parameterisation structure. The model setup is very simple, using a single steady ocean profile on zero-flow ocean boundaries and no surface forcing, which makes the melting simpler to parameterise than if a fully realistic ocean model were used. Despite these limitations, our proposed usage case is that the parameterisation could replace the need for a coupled ocean model, and so it seems reasonable to use such a model configuration as the comparator. A final note of caution is that the parameterisation structures recommended here may have undesirable consequences when used to drive an ice sheet model, and this remains to be tested.

5 Conclusions

This study uses high-resolution ocean model simulations to understand the processes controlling melting of ice shelves in the eastern Amundsen Sea. The highest melt rates are found in four ‘hot spots’ of melting where the main glacier trunks enter the ice shelves, accounting for 50% of the total meltwater flux from the region. This rapid melting occurs because the ice base sits in deep warm water and is steeply sloping, leading to rapid meltwater currents that sustain a high turbulent heat flux towards the ice. Secondary areas of elevated melting occur in shallower ice due to fast-flowing ‘meltwater outflows’, where the meltwater emanating from the hot spots is guided along slopes in the ice base by Coriolis force. The hot spots are located in regions that offer high ice-shelf buttressing near grounding lines, while the meltwater outflows are located beneath buttressing shear margins. These processes therefore sit at the centre of the (widely-proposed but still uncertain) chain of causation between anthropogenic climate change, Amundsen Sea ocean warming, increased ice-shelf melting, glacier acceleration, and sea-level rise.

These model results are then used to calibrate and test a variety of simple local parameterisations of melting that could be used in a stand-alone ice sheet model. The best-performing parameterisation states that ice-shelf melting is a function of temperature to the 3/2 power and ice-base slope to the 1/2 power, and tapers to zero within 3 kilometres of the grounding line. A more traditional law that is quadratic in temperature also performs well, with both formulations able to capture ~65% of the spatial pattern in the modelled melt fields. Both of these formulations also capture a strong melting feedback that takes place as Thwaites Glacier grounding line retreats. If the best-performing parameterisation is accurate, this implies 1) a nonlinear sensitivity of melting to ocean warming; 2) a melting feedback as the grounding line moves into deeper water, exposing more of the ice base to warm ocean forcing; 3) a feedback as melting steepens the ice-base slope; 4) ice-shelf melting that declines near grounding lines.

The parameterisations tested are able to capture the melting hot spots, and may therefore be used to model changes in buttressing near grounding lines, but they cannot capture the meltwater outflows along buttressing shear margins. This important limitation occurs because the ocean temperature driving melting is simple to parameterise through a linear dependence on the far-field temperature, while the sub-ice ocean current patterns are much harder to represent. Further improvements in parameterisation will require progress in simply representing meltwater currents rising along the ice base under the influence of Coriolis force. It is important to highlight that all of these conclusions are only applicable to the Amundsen Sea, and are dependent upon the simplifications applied to the modelling setup used for testing here. These model results are freely available for others to test more advanced parameterisations.

Code and data availability

Coupling scripts and model input files are available at https://drive.google.com/file/d/1I9HTRmPMIgyBTq0buaqDOmGDzRu0ndR0/view?usp=sharing and will be made available on Zenodo upon publication of the paper. The model output underlying the figures and calculations in this paper are available at https://drive.google.com/file/d/1NqA8jJ5LnFZhSSmNUF1rYkc7lCUR5Tj_/view?usp=sharing and will be made available through the UK Polar Data Centre upon publication of the paper.

Author contributions

PRH set up ocean models, performed simulations, performed analysis and led the manuscript writing. AJ guided the development of the melting parameterisation theory. DTB provided advice and data for future ice geometries. SLB provided advice and data for high-resolution ice shelf surface elevation. All authors contributed to writing the manuscript.

Competing interests

The contact author has declared that none of the authors has any competing interests.

Acknowledgements

This work used the ARCHER2 UK National Supercomputing Service (https://www.archer2.ac.uk).

Financial support

PRH was partly funded by SUNSET (UKRI-NERC: grant reference NE/X014061/1). AJ was partly funded by RASP (UKRI-NERC: grant reference NE/Y001451/1). DTB was partly funded by IceDice (UKRI-NERC: grant reference UKRI1276).

References

Anselin, J., Holland, P. R., Jenkins, A., and Taylor, J. R.: Ice Base Slope Effects on the Turbulent Ice Shelf–Ocean Boundary Current, J Phys Oceanogr, 54, 1545-1562, 10.1175/JPO-D-23-0256.1, 2024.

Arthern, R. J., and Williams, C. R.: The sensitivity of West Antarctica to the submarine melting feedback, Geophys Res Lett, 44, 2352-2359, 10.1002/2017gl072514, 2017.

Begeman, C. B., Tulaczyk, S. M., Marsh, O. J., Mikucki, J. A., Stanton, T. P., Hodson, T. O., Siegfried, M. R., Powell, R. D., Christianson, K., and King, M. A.: Ocean Stratification and Low Melt Rates at the Ross Ice Shelf Grounding Zone, Journal of Geophysical Research: Oceans, 123, 7438-7452, 10.1029/2018JC013987, 2018.

Bett, D. T., Holland, P. R., Naveira Garabato, A. C., Jenkins, A., Dutrieux, P., Kimura, S., and Fleming, A.: The impact of the Amundsen Sea freshwater balance on ocean melting of the West Antarctic Ice Sheet., J Geophys Res, 125, e2020JC016305, 10.1029/2020JC016305, 2020.

Bett, D. T., Bradley, A. T., Williams, C. R., Holland, P. R., Arthern, R. J., and Goldberg, D. N.: Coupled ice–ocean interactions during future retreat of West Antarctic ice streams in the Amundsen Sea sector, Cryosphere, 18, 2653-2675, 10.5194/tc-18-2653-2024, 2024.

Bevan, S. L., Luckman, A. J., Benn, D. I., Adusumilli, S., and Crawford, A.: Brief communication: Thwaites Glacier cavity evolution, Cryosphere, 15, 3317-3328, 10.5194/tc-15-3317-2021, 2021.

Burgard, C., Jourdain, N. C., Reese, R., Jenkins, A., and Mathiot, P.: An assessment of basal melt parameterisations for Antarctic ice shelves, Cryosphere, 16, 4931-4975, 10.5194/tc-16-4931-2022, 2022.

Burgard, C., Jourdain, N. C., Mathiot, P., Smith, R. S., Schäfer, R., Caillet, J., Finn, T. S., and Johnson, J. E.: Emulating Present and Future Simulations of Melt Rates at the Base of Antarctic Ice Shelves With Neural Networks, Journal of Advances in Modeling Earth Systems, 15, e2023MS003829, 10.1029/2023MS003829, 2023.

Chartrand, A. M., Howat, I. M., Joughin, I. R., and Smith, B. E.: Thwaites Glacier thins and retreats fastest where ice-shelf channels intersect its grounding zone, Cryosphere, 18, 4971-4992, 10.5194/tc-18-4971-2024, 2024.

Coulon, V., Klose, A. K., Kittel, C., Edwards, T., Turner, F., Winkelmann, R., and Pattyn, F.: Disentangling the drivers of future Antarctic ice loss with a historically calibrated ice-sheet model, Cryosphere, 18, 653-681, 10.5194/tc-18-653-2024, 2024.

Davis, P. E. D., Jenkins, A., Nicholls, K. W., Brennan, P. V., Abrahamsen, E. P., Heywood, K. J., Dutrieux, P., Cho, K. H., and Kim, T. W.: Variability in Basal Melting Beneath Pine Island Ice Shelf on Weekly to Monthly Timescales, J Geophys Res, 123, 8655-8669, 10.1029/2018jc014464, 2018.

Davis, P. E. D., Nicholls, K. W., Holland, D. M., Schmidt, B. E., Washam, P., Riverman, K. L., Arthern, R. J., Vaňková, I., Eayrs, C., Smith, J. A., Anker, P. G. D., Mullen, A. D., Dichek, D., Lawrence, J. D., Meister, M. M., Clyne, E., Basinski-Ferris, A., Rignot, E., Queste, B. Y., Boehme, L., Heywood, K. J., Anandakrishnan, S., and Makinson, K.: Suppressed basal melting in the eastern Thwaites Glacier grounding zone, Nature, 614, 479-485, 10.1038/s41586-022-05586-0, 2023.

Davis, P. E. D., Nicholls, K. W., Holland, D. M., Schmidt, B. E., Washam, P., Castro, B. F., Riverman, K. L., Smith, J. A., Anker, P. G. D., Mullen, A. D., Dichek, D., Clyne, E., and Makinson, K.: Lateral Fluxes Drive Basal Melting Beneath Thwaites Eastern Ice Shelf, West Antarctica, Geophys Res Lett, 52, e2024GL111873, 10.1029/2024GL111873, 2025.

De Rydt, J., Holland, P. R., Dutrieux, P., and Jenkins, A.: Geometric and oceanographic controls on melting beneath Pine Island Glacier, J Geophys Res, 119, 2420-2438, 10.1002/2013JC009513, 2014.

De Rydt, J., and Gudmundsson, G. H.: Coupled ice shelf-ocean modeling and complex grounding line retreat from a seabed ridge, J Geophys Res-Earth, 121, 865-880, 10.1002/2015jf003791, 2016.

De Rydt, J., and Naughten, K.: Geometric amplification and suppression of ice-shelf basal melt in West Antarctica, Cryosphere, 18, 1863-1888, 10.5194/tc-18-1863-2024, 2024.

Dutrieux, P., Vaughan, D. G., Corr, H. F. J., Jenkins, A., Holland, P. R., Joughin, I., and Fleming, A. H.: Pine Island Glacier ice shelf melt distributed at kilometre scales, Cryosphere, 7, 1543-1555, 10.5194/tc-7-1543-2013, 2013.

Dutrieux, P., De Rydt, J., Jenkins, A., Holland, P. R., Ha, H. K., Lee, S. H., Steig, E. J., Ding, Q. H., Abrahamsen, E. P., and Schroder, M.: Strong Sensitivity of Pine Island Ice-Shelf Melting to Climatic Variability, Science, 343, 174-178, 10.1126/science.1244341, 2014.

Favier, L., Durand, G., Cornford, S. L., Gudmundsson, G. H., Gagliardini, O., Gillet-Chaulet, F., Zwinger, T., Payne, A. J., and Le Brocq, A. M.: Retreat of Pine Island Glacier controlled by marine ice-sheet instability, Nat Clim Change, 4, 117-121, 10.1038/nclimate2094, 2014.

Favier, L., Jourdain, N. C., Jenkins, A., Merino, N., Durand, G., Gagliardini, O., Gillet-Chaulet, F., and Mathiot, P.: Assessment of sub-shelf melting parameterisations using the ocean-ice-sheet coupled model NEMO(v3.6)-Elmer/Ice(v8.3), Geosci Model Dev, 12, 2255-2283, 10.5194/gmd-12-2255-2019, 2019.

Finucane, G., and Stewart, A. L.: A Predictive Theory for Heat Transport Into Ice Shelf Cavities, Geophys Res Lett, 51, e2024GL108196, 10.1029/2024GL108196, 2024.

Goldberg, D. N., Gourmelen, N., Kimura, S., Millan, R., and Snow, K.: How Accurately Should We Model Ice Shelf Melt Rates?, Geophys Res Lett, 46, 189-199, 10.1029/2018GL080383, 2019.

González, C., Bachmann, M., Bueso-Bello, J.-L., Rizzoli, P., and Zink, M.: A Fully Automatic Algorithm for Editing the TanDEM-X Global DEM, Remote Sens-Basel, 12, 3961, 2020.

Gourmelen, N., Goldberg, D. N., Snow, K., Henley, S. F., Bingham, R. G., Kimura, S., Hogg, A. E., Shepherd, A., Mouginot, J., Lenaerts, J. T. M., Ligtenberg, S. R. M., and van de Berg, W. J.: Channelized Melting Drives Thinning Under a Rapidly Melting Antarctic Ice Shelf, Geophys Res Lett, 44, 9796-9804, 10.1002/2017GL074929, 2017.

Gourmelen, N., Jakob, L., Holland, P. R., Dutrieux, P., Goldberg, D., Bevan, S., Luckman, A., and Malczyk, G.: The influence of subglacial lake discharge on Thwaites Glacier ice-shelf melting and grounding-line retreat, Nat Commun, 16, 2272, 10.1038/s41467-025-57417-1, 2025.

Gudmundsson, G. H., Barnes, J. M., Goldberg, D. N., and Morlighem, M.: Limited Impact of Thwaites Ice Shelf on Future Ice Loss From Antarctica, Geophys Res Lett, 50, e2023GL102880, 10.1029/2023GL102880, 2023.

Holland, P. R., and Feltham, D. L.: The effects of rotation and ice shelf topography on frazil-laden ice shelf water plumes, J Phys Oceanogr, 36, 2312-2327, 10.1175/Jpo2970.1, 2006.

Holland, P. R.: A model of tidally dominated ocean processes near ice shelf grounding lines, J Geophys Res, 113, C11002, 10.1029/2007jc004576, 2008.

Holland, P. R., Jenkins, A., and Holland, D. M.: The response of ice shelf basal melting to variations in ocean temperature, J Climate, 21, 2558-2572, 10.1175/2007jcli1909.1, 2008.

Holland, P. R., O'Connor, G. K., Bracegirdle, T. J., Dutrieux, P., Naughten, K. A., Steig, E. J., Schneider, D. P., Jenkins, A., and Smith, J. A.: Anthropogenic and internal drivers of wind changes over the Amundsen Sea, West Antarctica, during the 20th and 21st centuries, Cryosphere, 16, 5085-5105, 10.5194/tc-16-5085-2022, 2022.

Holland, P. R., Bevan, S. L., and Luckman, A. J.: Strong Ocean Melting Feedback During the Recent Retreat of Thwaites Glacier, Geophys Res Lett, 50, e2023GL103088, 10.1029/2023GL103088, 2023.

Horgan, H. J., Stewart, C., Stevens, C., Dunbar, G., Balfoort, L., Schmidt, B. E., Washam, P., Werder, M. A., Mandeno, D., Marschalek, J., Hulbe, C., Holschuh, N., Levy, R., Hurwitz, B., Jendersie, S., Johnson, K., Lawrence, J., Morgenstern, R., Mullen, A. D., Quartini, E., Sauthoff, W., Siegfried, M., Still, H., Thorpe-Loversuch, S., van de Flierdt, T., Venturelli, R., and Whiteford, A.: A West Antarctic grounding-zone environment shaped by episodic water flow, Nat Geosci, 18, 389-395, 10.1038/s41561-025-01687-3, 2025.

IPCC: Summary for Policymakers, in: Climate Change 2021: The Physical Science Basis. Contribution of Working Group I to the Sixth Assessment Report of the Intergovernmental Panel on Climate Change, edited by: Masson-Delmotte, V., Zhai, P., Pirani, A., Connors, S. L., Péan, C., Berger, S., Caud, N., Chen, Y., Goldfarb, L., Gomis, M. I., Huang, M., Leitzell, K., Lonnoy, E., Matthews, J. B. R., Maycock, T. K., Waterfield, T., Yelekçi, O., Yu, R., and Zhou, B., Cambridge University Press, Cambridge, United Kingdom and New York, NY, USA, 3−32, 2021.

Jacobs, S., Jenkins, A., Hellmer, H., Giulivi, C., Nitsche, F., Huber, B., and Guerrero, R.: The Amundsen Sea and the Antarctic Ice Sheet, Oceanography, 25, 154-163, 2012.

Jenkins, A.: A One-Dimensional Model of Ice Shelf-Ocean Interaction, J Geophys Res, 96, 20671-20677, 1991.

Jenkins, A., Nicholls, K. W., and Corr, H. F. J.: Observation and Parameterization of Ablation at the Base of Ronne Ice Shelf, Antarctica, J Phys Oceanogr, 40, 2298-2312, 10.1175/2010jpo4317.1, 2010.

Jenkins, A.: Convection-Driven Melting near the Grounding Lines of Ice Shelves and Tidewater Glaciers, J Phys Oceanogr, 41, 2279-2294, 10.1175/Jpo-D-11-03.1, 2011.

Jenkins, A.: A Simple Model of the Ice Shelf-Ocean Boundary Layer and Current, J Phys Oceanogr, 46, 1785-1803, 10.1175/Jpo-D-15-0194.1, 2016.

Jenkins, A., Shoosmith, D., Dutrieux, P., Jacobs, S., Kim, T. W., Lee, S. H., Ha, H. K., and Stammerjohn, S.: West Antarctic Ice Sheet retreat in the Amundsen Sea driven by decadal oceanic variability, Nat Geosci, 11, 733-738, 10.1038/s41561-018-0207-4, 2018.

Jenkins, A.: Interaction of ice shelves with the ocean, in: Glaciers and Ice Sheets in the Climate System, edited by: Fowler, A., and Ng, F., Springer, 93-130, 2021a.

Jenkins, A.: Shear, Stability, and Mixing within the Ice Shelf–Ocean Boundary Current, J Phys Oceanogr, 51, 2129-2148, 10.1175/JPO-D-20-0096.1, 2021b.

Jordan, T. A., Porter, D., Tinto, K., Millan, R., Muto, A., Hogan, K., Larter, R. D., Graham, A. G. C., and Paden, J. D.: New gravity-derived bathymetry for the Thwaites, Crosson, and Dotson ice shelves revealing two ice shelf populations, Cryosphere, 14, 2869-2882, 10.5194/tc-14-2869-2020, 2020.

Joughin, I., Smith, B. E., and Medley, B.: Marine Ice Sheet Collapse Potentially Under Way for the Thwaites Glacier Basin, West Antarctica, Science, 344, 735-738, 10.1126/science.1249055, 2014.

Joughin, I., Shapero, D., Dutrieux, P., and Smith, B.: Ocean-induced melt volume directly paces ice loss from Pine Island Glacier, Science Advances, 7, eabi5738, doi:10.1126/sciadv.abi5738, 2021.

Jourdain, N. C., Asay-Davis, X., Hattermann, T., Straneo, F., Seroussi, H., Little, C. M., and Nowicki, S.: A protocol for calculating basal melt rates in the ISMIP6 Antarctic ice sheet projections, Cryosphere, 14, 3111-3134, 10.5194/tc-14-3111-2020, 2020.

Kimura, S., Jenkins, A., Regan, H., Holland, P. R., Assmann, K. M., Whitt, D. B., Van Wessem, M., van de Berg, W. J., Reijmer, C. H., and Dutrieux, P.: Oceanographic Controls on the Variability of Ice-Shelf Basal Melting and Circulation of Glacial Meltwater in the Amundsen Sea Embayment, Antarctica, J Geophys Res, 122, 10131-10155, 10.1002/2017jc012926, 2017.

Konrad, H., Gilbert, L., Cornford, S. L., Payne, A. J., Hogg, A., Muir, A., and Shepherd, A.: Uneven onset and pace of ice-dynamical imbalance in the Amundsen Sea Embayment, West Antarctica, Geophys Res Lett, 44, 910-918, 10.1002/2016GL070733, 2017.

Lambert, E., Jüling, A., van de Wal, R. S. W., and Holland, P. R.: Modelling Antarctic ice shelf basal melt patterns using the one-layer Antarctic model for dynamical downscaling of ice–ocean exchanges (LADDIE v1.0), Cryosphere, 17, 3203-3228, 10.5194/tc-17-3203-2023, 2023.

Lambert, E., and Burgard, C.: Brief communication: Sensitivity of Antarctic ice shelf melting to ocean warming across basal melt models, Cryosphere, 19, 2495-2505, 10.5194/tc-19-2495-2025, 2025.

Lazeroms, W. M. J., Jenkins, A., Gudmundsson, G. H., and van de Wal, R. S. W.: Modelling present-day basal melt rates for Antarctic ice shelves using a parametrization of buoyant meltwater plumes, Cryosphere, 12, 49-70, 10.5194/tc-12-49-2018, 2018.

Lazeroms, W. M. J., Jenkins, A., Rienstra, S. W., and van de Wal, R. S. W.: An Analytical Derivation of Ice-Shelf Basal Melt Based on the Dynamics of Meltwater Plumes, J Phys Oceanogr, 49, 917-939, 10.1175/jpo-d-18-0131.1, 2019.

Le Brocq, A. M., Ross, N., Griggs, J. A., Bingham, R. G., Corr, H. F. J., Ferraccioli, F., Jenkins, A., Jordan, T. A., Payne, A. J., Rippin, D. M., and Siegert, M. J.: Evidence from ice shelves for channelized meltwater flow beneath the Antarctic Ice Sheet, Nat Geosci, 6, 945-948, 10.1038/ngeo1977, 2013.

Lhermitte, S., Sun, S., Shuman, C., Wouters, B., Pattyn, F., Wuite, J., Berthier, E., and Nagler, T.: Damage accelerates ice shelf instability and mass loss in Amundsen Sea Embayment, Proceedings of the National Academy of Sciences, 117, 24,735-724,741, 10.1073/pnas.1912890117, 2020.

Losch, M.: Modeling ice shelf cavities in a z coordinate ocean general circulation model, J Geophys Res, 113, C08043, 10.1029/2007jc004368, 2008.

Lowery, K., Dutrieux, P., Holland, P. R., Hogg, A. E., Gourmelen, N., and Wallis, B. J.: Spatio-temporal melt and basal channel evolution on Pine Island Glacier ice shelf from CryoSat-2, Cryosphere, 19, 4893-4911, 10.5194/tc-19-4893-2025, 2025.

Lowery, K., Holland, P. R., Dutrieux, P., Hogg, A. E., and Gourmelen, N.: Drivers of basal melt variability for Pine Island Glacier Ice Shelf: Ocean forcing versus geometric feedback, Geophys Res Lett, submitted.

MacAyeal, D. R.: Thermohaline Circulation Below the Ross Ice Shelf - a Consequence of Tidally Induced Vertical Mixing and Basal Melting, J Geophys Res, 89, 597-606, 10.1029/Jc089ic01p00597, 1984.

Mallett, H. K. W., Boehme, L., Fedak, M., Heywood, K. J., Stevens, D. P., and Roquet, F.: Variation in the Distribution and Properties of Circumpolar Deep Water in the Eastern Amundsen Sea, on Seasonal Timescales, Using Seal-Borne Tags, Geophys Res Lett, 45, 4982-4990, 10.1029/2018GL077430, 2018.

Mankoff, K. D., Jacobs, S. S., Tulaczyk, S. M., and Stammerjohn, S. E.: The role of Pine Island Glacier ice shelf basal channels in deep-water upwelling, polynyas and ocean circulation in Pine Island Bay, Antarctica, Ann Glaciol, 53, 123-128, Doi 10.3189/2012aog60a062, 2012.

Miles, B., Stokes, C., Jenkins, A., Jordan, J., Jamieson, S., and Gudmundsson, G.: Intermittent structural weakening and acceleration of the Thwaites Glacier Tongue between 2000 and 2018, J Glaciol, 66, 485-495, 10.1017/jog.2020.20, 2020.

Milillo, P., Rignot, E., Rizzoli, P., Scheuchl, B., Mouginot, J., Bueso-Bello, J., and Prats-Iraola, P.: Heterogeneous retreat and ice melt of Thwaites Glacier, West Antarctica, Science Advances, 5, eaau3433, 10.1126/sciadv.aau3433, 2019.

Minowa, M., Sugiyama, S., Ito, M., Yamane, S., and Aoki, S.: Thermohaline structure and circulation beneath the Langhovde Glacier ice shelf in East Antarctica, Nat Commun, 12, 4209, 10.1038/s41467-021-23534-w, 2021.

Morlighem, M., Rignot, E., Binder, T., Blankenship, D., Drews, R., Eagles, G., Eisen, O., Ferraccioli, F., Forsberg, R., Fretwell, P., Goel, V., Greenbaum, J. S., Gudmundsson, H., Guo, J. X., Helm, V., Hofstede, C., Howat, I., Humbert, A., Jokat, W., Karlsson, N. B., Lee, W. S., Matsuoka, K., Millan, R., Mouginot, J., Paden, J., Pattyn, F., Roberts, J., Rosier, S., Ruppel, A., Seroussi, H., Smith, E. C., Steinhage, D., Sun, B., van den Broeke, M. R., van Ommen, T. D., van Wessem, M., and Young, D. A.: Deep glacial troughs and stabilizing ridges unveiled beneath the margins of the Antarctic ice sheet, Nat Geosci, 13, 132-137, 10.1038/s41561-019-0510-8, 2020.

Morlighem, M., Goldberg, D., Dias dos Santos, T., Lee, J., and Sagebaum, M.: Mapping the Sensitivity of the Amundsen Sea Embayment to Changes in External Forcings Using Automatic Differentiation, Geophys Res Lett, 48, e2021GL095440, 10.1029/2021GL095440, 2021.

Mouginot, J., Rignot, E., and Scheuchl, B.: Sustained increase in ice discharge from the Amundsen Sea Embayment, West Antarctica, from 1973 to 2013, Geophys Res Lett, 41, 1576-1584, 10.1002/2013gl059069, 2014.

Nakayama, Y., Schroder, M., and Hellmer, H. H.: From circumpolar deep water to the glacial meltwater plume on the eastern Amundsen Shelf, Deep-Sea Res I, 77, 50-62, 10.1016/j.dsr.2013.04.001, 2013.

Nakayama, Y., Manucharyan, G., Zhang, H., Dutrieux, P., Torres, H. S., Klein, P., Seroussi, H., Schodlok, M., Rignot, E., and Menemenlis, D.: Pathways of ocean heat towards Pine Island and Thwaites grounding lines, Scientific Reports, 9, 16649, 10.1038/s41598-019-53190-6, 2019.

Nakayama, Y., Cai, C., and Seroussi, H.: Impact of Subglacial Freshwater Discharge on Pine Island Ice Shelf, Geophys Res Lett, 48, e2021GL093923, 10.1029/2021GL093923, 2021.

Naughten, K. A., Holland, P. R., Dutrieux, P., Kimura, S., Bett, D. T., and Jenkins, A.: Simulated twentieth-century ocean warming in the Amundsen Sea, West Antarctica, Geophys Res Lett, 49, e2021GL094566, 10.1029/2021GL094566, 2022.

Naughten, K. A., Holland, P. R., and De Rydt, J.: Unavoidable future increase in West Antarctic ice-shelf melting over the twenty-first century, Nat Clim Change, 13, 1222-1228, 10.1038/s41558-023-01818-x, 2023.

Naveira Garabato, A. C., Forryan, A., Dutrieux, P., Brannigan, L., Biddle, L. C., Heywood, K. J., Jenkins, A., Firing, Y. L., and Kimura, S.: Vigorous lateral export of the meltwater outflow from beneath an Antarctic ice shelf, Nature, 542, 219-222, 10.1038/nature20825, 2017.

Nias, I. J., Cornford, S. L., Edwards, T. L., Gourmelen, N., and Payne, A. J.: Assessing Uncertainty in the Dynamical Ice Response to Ocean Warming in the Amundsen Sea Embayment, West Antarctica, Geophys Res Lett, 46, 11253-11260, 10.1029/2019GL084941, 2019.

Nicola, L., Reese, R., Kreuzer, M., Albrecht, T., and Winkelmann, R.: Bathymetry-constrained warm-mode melt estimates derived from analysing oceanic gateways in Antarctica, Cryosphere, 19, 2263-2287, 10.5194/tc-19-2263-2025, 2025.

O'Connor, G. K., Holland, P. R., Steig, E. J., Dutrieux, P., and Hakim, G. J.: Characteristics and rarity of the strong 1940s westerly wind event over the Amundsen Sea, West Antarctica, Cryosphere, 17, 4399-4420, 10.5194/tc-17-4399-2023, 2023.

Olbers, D., and Hellmer, H.: A box model of circulation and melting in ice shelf caverns, Ocean Dynam, 60, 141-153, 10.1007/s10236-009-0252-z, 2010.

Otosaka, I. N., Shepherd, A., Ivins, E. R., Schlegel, N. J., Amory, C., van den Broeke, M. R., Horwath, M., Joughin, I., King, M. D., Krinner, G., Nowicki, S., Payne, A. J., Rignot, E., Scambos, T., Simon, K. M., Smith, B. E., Sørensen, L. S., Velicogna, I., Whitehouse, P. L., A, G., Agosta, C., Ahlstrøm, A. P., Blazquez, A., Colgan, W., Engdahl, M. E., Fettweis, X., Forsberg, R., Gallée, H., Gardner, A., Gilbert, L., Gourmelen, N., Groh, A., Gunter, B. C., Harig, C., Helm, V., Khan, S. A., Kittel, C., Konrad, H., Langen, P. L., Lecavalier, B. S., Liang, C. C., Loomis, B. D., McMillan, M., Melini, D., Mernild, S. H., Mottram, R., Mouginot, J., Nilsson, J., Noël, B., Pattle, M. E., Peltier, W. R., Pie, N., Roca, M., Sasgen, I., Save, H. V., Seo, K. W., Scheuchl, B., Schrama, E. J. O., Schröder, L., Simonsen, S. B., Slater, T., Spada, G., Sutterley, T. C., Vishwakarma, B. D., van Wessem, J. M., Wiese, D., van der Wal, W., and Wouters, B.: Mass balance of the Greenland and Antarctic ice sheets from 1992 to 2020, Earth Syst. Sci. Data, 15, 1597-1616, 10.5194/essd-15-1597-2023, 2023.

Patmore, R. D., Holland, P. R., Vreugdenhil, C. A., Jenkins, A., and Taylor, J. R.: Turbulence in the Ice Shelf–Ocean Boundary Current and Its Sensitivity to Model Resolution, J Phys Oceanogr, 53, 613-633, 10.1175/JPO-D-22-0034.1, 2023.

Payne, A. J., Holland, P. R., Shepherd, A. P., Rutt, I. C., Jenkins, A., and Joughin, I.: Numerical modeling of ocean-ice interactions under Pine Island Bay's ice shelf, J Geophys Res, 112, C10019, 10.1029/2006jc003733, 2007.

Poinelli, M., Siegelman, L., Nakayama, Y., Rignot, E., Seroussi, H., Fenty, I., and Larour, E.: Small-Scale, High-Frequency Ice, and Ocean Processes in the Amundsen Sea Embayment, West Antarctica, Journal of Advances in Modeling Earth Systems, 17, e2025MS005098, 10.1029/2025MS005098, 2025.

Reed, B., Green, J. A. M., Jenkins, A., and Gudmundsson, G. H.: Recent irreversible retreat phase of Pine Island Glacier, Nat Clim Change, 14, 75-81, 10.1038/s41558-023-01887-y, 2024.

Reese, R., Albrecht, T., Mengel, M., Asay-Davis, X., and Winkelmann, R.: Antarctic sub-shelf melt rates via PICO, Cryosphere, 12, 1969-1985, 10.5194/tc-12-1969-2018, 2018a.

Reese, R., Gudmundsson, G. H., Levermann, A., and Winkelmann, R.: The far reach of ice-shelf thinning in Antarctica, Nat Clim Change, 8, 53-57, 10.1038/s41558-017-0020-x, 2018b.

Rignot, E., Mouginot, J., Scheuchl, B., van den Broeke, M. R., van Wessem, M. J., and Morlighem, M.: Four decades of Antarctic Ice Sheet mass balance from 1979–2017, Proceedings of the National Academy of Sciences, 116, 1095-1103, 10.1073/pnas.1812883116, 2019.

Rignot, E., Ciracì, E., Scheuchl, B., Tolpekin, V., Wollersheim, M., and Dow, C.: Widespread seawater intrusions beneath the grounded ice of Thwaites Glacier, West Antarctica, Proceedings of the National Academy of Sciences, 121, e2404766121, 10.1073/pnas.2404766121, 2024.

Rosevear, M. G., Gayen, B., Vreugdenhil, C. A., and Galton-Fenzi, B. K.: How Does the Ocean Melt Antarctic Ice Shelves?, Annu Rev Mar Sci, 17, 325-353, 10.1146/annurev-marine-040323-074354, 2025.

Rosier, S. H. R., Bull, C. Y. S., Woo, W. L., and Gudmundsson, G. H.: Predicting ocean-induced ice-shelf melt rates using deep learning, Cryosphere, 17, 499-518, 10.5194/tc-17-499-2023, 2023.

Savidge, E., Snow, T., and Siegfried, M. R.: Multi-Decadal Record of Sensible-Heat Polynya Variability From Satellite Optical and Thermal Imagery at Pine Island Glacier, West Antarctica, Geophys Res Lett, 50, e2023GL106178, 10.1029/2023GL106178, 2023.

Schmidt, B. E., Washam, P., Davis, P. E. D., Nicholls, K. W., Holland, D. M., Lawrence, J. D., Riverman, K. L., Smith, J. A., Spears, A., Dichek, D. J. G., Mullen, A. D., Clyne, E., Yeager, B., Anker, P., Meister, M. R., Hurwitz, B. C., Quartini, E. S., Bryson, F. E., Basinski-Ferris, A., Thomas, C., Wake, J., Vaughan, D. G., Anandakrishnan, S., Rignot, E., Paden, J., and Makinson, K.: Heterogeneous melting near the Thwaites Glacier grounding line, Nature, 614, 471-478, 10.1038/s41586-022-05691-0, 2023.

Selley, H. L., Hogg, A. E., Davison, B. J., Dutrieux, P., and Slater, T.: Speed-up, slowdown, and redirection of ice flow on neighbouring ice streams in the Pope, Smith, and Kohler region of West Antarctica, Cryosphere, 19, 1725-1738, 10.5194/tc-19-1725-2025, 2025.

Seroussi, H., Nakayama, Y., Larour, E., Menemenlis, D., Morlighem, M., Rignot, E., and Khazendar, A.: Continued retreat of Thwaites Glacier, West Antarctica, controlled by bed topography and ocean circulation, Geophys Res Lett, 44, 6191–6199, 10.1002/2017GL072910, 2017.

Seroussi, H., Verjans, V., Nowicki, S., Payne, A. J., Goelzer, H., Lipscomb, W. H., Abe-Ouchi, A., Agosta, C., Albrecht, T., Asay-Davis, X., Barthel, A., Calov, R., Cullather, R., Dumas, C., Galton-Fenzi, B. K., Gladstone, R., Golledge, N. R., Gregory, J. M., Greve, R., Hattermann, T., Hoffman, M. J., Humbert, A., Huybrechts, P., Jourdain, N. C., Kleiner, T., Larour, E., Leguy, G. R., Lowry, D. P., Little, C. M., Morlighem, M., Pattyn, F., Pelle, T., Price, S. F., Quiquet, A., Reese, R., Schlegel, N. J., Shepherd, A., Simon, E., Smith, R. S., Straneo, F., Sun, S., Trusel, L. D., Van Breedam, J., Van Katwyk, P., van de Wal, R. S. W., Winkelmann, R., Zhao, C., Zhang, T., and Zwinger, T.: Insights into the vulnerability of Antarctic glaciers from the ISMIP6 ice sheet model ensemble and associated uncertainty, Cryosphere, 17, 5197-5217, 10.5194/tc-17-5197-2023, 2023.

Shean, D. E., Joughin, I. R., Dutrieux, P., Smith, B. E., and Berthier, E.: Ice shelf basal melt rates from a high-resolution digital elevation model (DEM) record for Pine Island Glacier, Antarctica, Cryosphere, 13, 2633-2656, 10.5194/tc-13-2633-2019, 2019.

Shepherd, A., Wingham, D., and Rignot, E.: Warm ocean is eroding West Antarctic Ice Sheet, Geophys Res Lett, 31, L23402, 10.1029/2004gl021106, 2004.

Shepherd, A., Gilbert, L., Muir, A. S., Konrad, H., McMillan, M., Slater, T., Briggs, K. H., Sundal, A. V., Hogg, A. E., and Engdahl, M. E.: Trends in Antarctic Ice Sheet Elevation and Mass, Geophys Res Lett, 46, 8174-8183, 10.1029/2019gl082182, 2019.

Shrestha, K., Manucharyan, G. E., and Nakayama, Y.: Submesoscale Variability and Basal Melting in Ice Shelf Cavities of the Amundsen Sea, Geophys Res Lett, 51, e2023GL107029, 10.1029/2023GL107029, 2024.

Smith, J. A., Andersen, T. J., Shortt, M., Gaffney, A. M., Truffer, M., Stanton, T. P., Bindschadler, R., Dutrieux, P., Jenkins, A., Hillenbrand, C. D., Ehrmann, W., Corr, H. F. J., Farley, N., Crowhurst, S., and Vaughan, D. G.: Sub-ice-shelf sediments record history of twentieth-century retreat of Pine Island Glacier, Nature, 549, 292-292, 10.1038/nature23650, 2017.

Snow, K., Goldberg, D. N., Holland, P. R., Jordan, J. R., Arthern, R. J., and Jenkins, A.: The Response of Ice Sheets to Climate Variability, Geophys Res Lett, 44, 11878-11885, 10.1002/2017gl075745, 2017.

St-Laurent, P., Klinck, J. M., and Dinniman, M. S.: Impact of local winter cooling on the melt of Pine Island Glacier, Antarctica, J Geophys Res, 120, 6718-6732, 10.1002/2015JC010709, 2015.

Thurnherr, A. M., Jacobs, S. S., Dutrieux, P., and Giulivi, C. F.: Export and circulation of ice cavity water in Pine Island Bay, West Antarctica, Journal of Geophysical Research: Oceans, 119, 1754-1764, 10.1002/2013JC009307, 2014.

Turner, K. A., Naughten, K. A., Holland, P. R., and Naveira Garabato, A. C.: Modeled Centennial Ocean Warming in the Amundsen Sea Driven by Thermodynamic Atmospheric Changes, Not Winds, Geophys Res Lett, 52, e2024GL112287, 10.1029/2024GL112287, 2025.

Vreugdenhil, C. A., and Taylor, J. R.: Stratification effects in the turbulent boundary layer beneath a melting ice shelf: insights from resolved large-eddy simulations, J Phys Oceanogr, 10.1175/JPO-D-18-0252.1, 2019.

Wild, C. T., Kachuck, S. B., Luckman, A., Alley, K. E., Sharp, M. A., Smith, H., Tyler, S. W., Kratt, C., Dotto, T. S., Price, D., Nicholls, K. W., Bevan, S. L., Collao-Barrios, G., Muto, A., Truffer, M., Scambos, T. A., Heywood, K. J., and Pettit, E. C.: Rift propagation signals the last act of the Thwaites Eastern Ice Shelf despite low basal melt rates, J Glaciol, 70, e21, 10.1017/jog.2024.64, 2024.

Yung, C. K., Asay-Davis, X. S., Adcroft, A., Bull, C. Y. S., De Rydt, J., Dinniman, M. S., Galton-Fenzi, B. K., Goldberg, D., Gwyther, D. E., Hallberg, R., Harrison, M., Hattermann, T., Holland, D. M., Holland, D., Holland, P. R., Jordan, J. R., Jourdain, N. C., Kusahara, K., Marques, G., Mathiot, P., Menemenlis, D., Morrison, A. K., Nakayama, Y., Sergienko, O., Smith, R. S., Stern, A., Timmermann, R., and Zhou, Q.: Results of the second Ice Shelf–Ocean Model Intercomparison Project (ISOMIP+), Cryosphere, 20, 2053-2088, 10.5194/tc-20-2053-2026, 2026.

Zheng, Y., Stevens, D. P., Heywood, K. J., Webber, B. G. M., and Queste, B. Y.: Reversal of ocean gyres near ice shelves in the Amundsen Sea caused by the interaction of sea ice and wind, Cryosphere, 16, 3005-3019, 10.5194/tc-16-3005-2022, 2022.

Zinck, A.-S. P., Lhermitte, S., Wearing, M. G., and Wouters, B.: Channelized melt beneath Antarctic ice shelves previously underestimated, Nat Clim Change, 16, 350-353, 10.1038/s41558-025-02537-1, 2026.

Zinck, A. S. P., Wouters, B., Lambert, E., and Lhermitte, S.: Unveiling spatial variability within the Dotson Melt Channel through high-resolution basal melt rates from the Reference Elevation Model of Antarctica, Cryosphere, 17, 3785-3801, 10.5194/tc-17-3785-2023, 2023.

symbol	value	description
c_d	0.0025	drag coefficient in momentum equation
c_i	2,000 J kg^{-1} °C^{-1}	specific heat capacity of ice
c_o	3,994 J kg^{-1} °C^{-1}	specific heat capacity of ocean
ε	-	ratio of mixing across the boundary layer to mixing across the pyncocline
f	-1.4×10^{-4} s^{-1}	Coriolis parameter
Γ_T	0.011	boundary layer heat transfer coefficient
Γ_S	3.1×10^{-4}	boundary layer salt transfer coefficient
$\Gamma_{\{TS\}}$	-	combined transfer coefficient
g	-9.81 m s^{-1}	acceleration due to gravity
L_i	334,000 J kg^{-1}	latent heat of ice fusion
λ_1	-0.0575 °C	slope of liquidus for seawater
λ_2	0.0901 °C	offset of liquidus for seawater
λ_3	7.61×10^{-8} °C Pa^{-1}	depression of freezing point with pressure for seawater
φ	1.97	melting multiplier used to tune melting parameterisation
P_0	-	ratio between meltwater density and thermal driving
ρ_i	917 kg m^{-3}	density of ice
ρ_o	1028.5 kg m^{-3}	density of seawater
T_i	-20 °C	internal ice shelf temperature

Table 1: Constants and parameters used in paper.

Parameterisation	Tuned coefficient C (various units)	Coefficient of Determination between spatial patterns of parameterised and modelled melting in present-day simulations (r^2)	Mean Absolute Error between parameterised and modelled melting in present-day simulations (m/y)
$m = C\left(T^r - T_f^r\right)^{3/2} (\sin\theta)^{1/2}\,\Psi(3\text{ km})$	40.3	0.649	5.45
$m = C\left(T^r - T_f^r\right)^{3/2} (\sin\theta)^{1/2}$	33.2	0.606	5.74
$m = C\left(T^r - T_f^r\right)^{3/2}$	6.57	0.583	5.94
$m = C\left(T^r - T_f^r\right)^{2} \sin\theta\ \ \Psi(3\text{ km})$	86.9	0.526	6.11
$m = C\left(T^r - T_f^r\right)^{2} \sin\theta$	69.5	0.478	6.45
$m = C\left(T^r - T_f^r\right)^{2}\Psi(3\text{ km})$	4.66	0.645	5.20
$m = C\left(T^r - T_f^r\right)^{2}$	3.71	0.596	5.55
$m = C\left(T^r - T_f^r\right)$	10.6	0.525	6.71
$m = Cz_b$	-0.0326	0.356	9.06

Table 2: Performance of tuned parameterisation. Each row shows the tuning of the parameterisation that is optimal to match melt rates in the reference present-day simulation, and then a set of metrics measuring the performance of that tuned parameterisation.

https://doi.org/10.5194/egusphere-2026-2835
Preprint. Discussion started: 2 June 2026

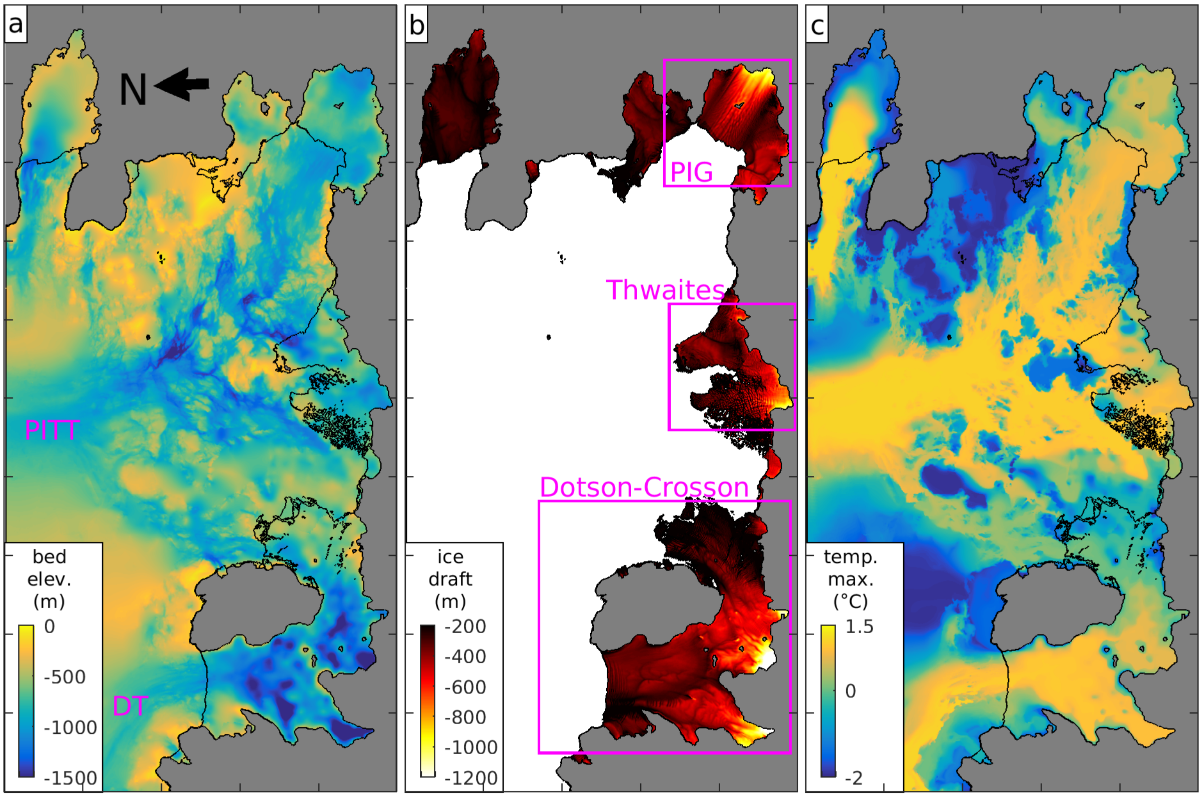

Figure 1: Domain geometry and temperature distribution. (a) Seabed elevation. (b) Ice shelf draft. (c) Maximum temperature at any depth in water column. Pink boxes in panel b show the ice-shelf zoom regions use in later figures. PITT: Pine Island—Thwaites Trough; DT: Dotson Trough. Axis ticks are every 50 km.

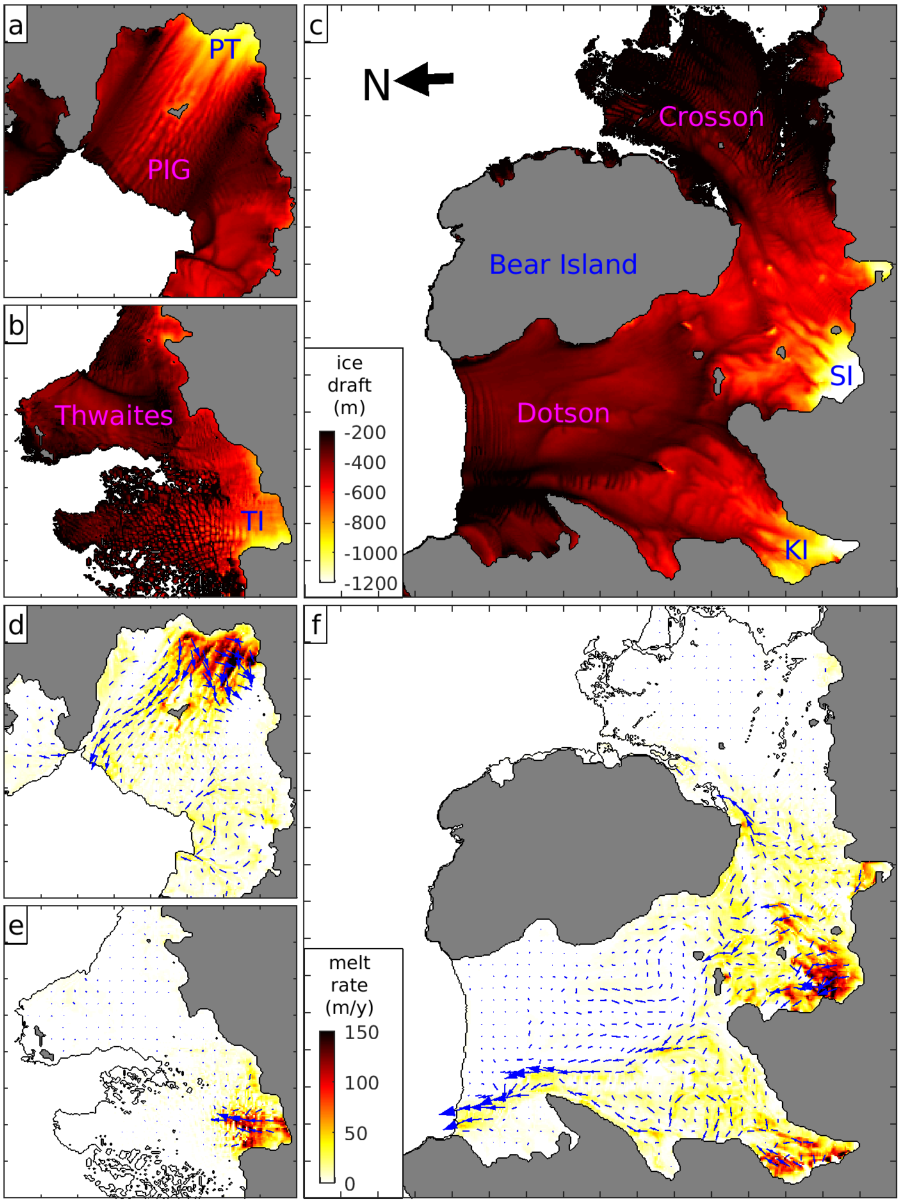

Figure 2: Ice draft, melt rates, and sub-ice currents. (a)-(c) Ice draft. (d)-(f) Melt rates and sub-ice currents. PT: PIG trunk, TI: Thwaites Inlet, KI: Kohler Inlet, SI: Smith Inlet. Despite this naming convention, we note that KI includes Horrall and Kohler West glaciers, while SI includes Kohler East, Smith West, and Smith East glaciers (Selley et al., 2025). Axis ticks are every 10 km.

https://doi.org/10.5194/egusphere-2026-2835
Preprint. Discussion started: 2 June 2026

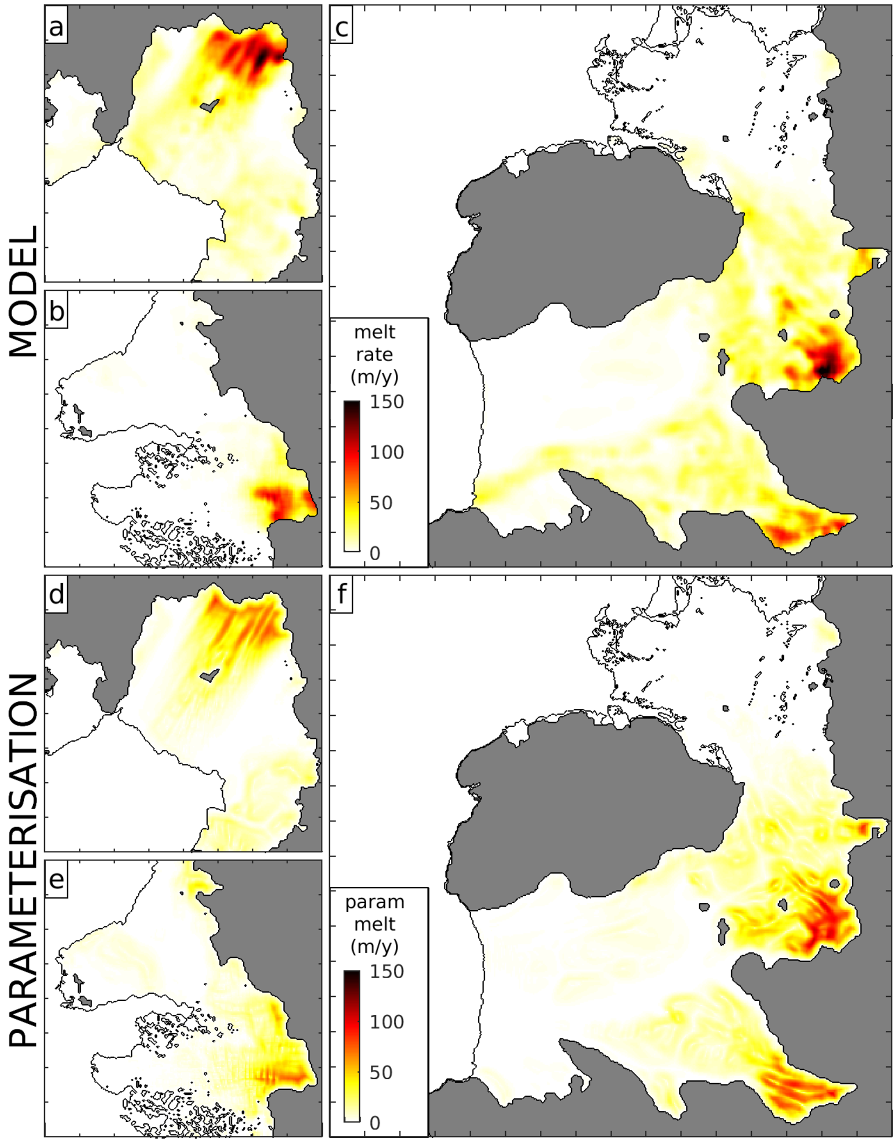

1025 **Figure 3: Modelled and parameterised melt rates.** (a)-(c) Modelled melt rates after smoothing with a 7×7 cell box-average filter. (d)-(f) Parameterised melt rates using the tuned best-fit expression (18).

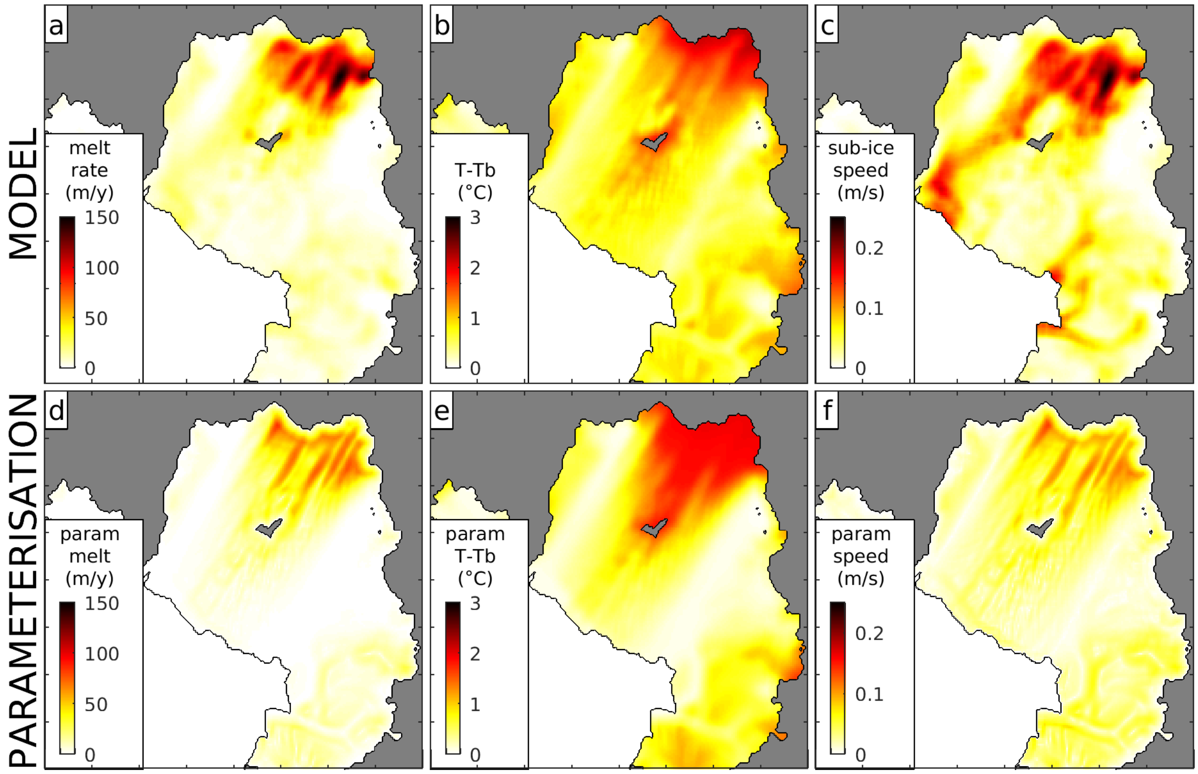

Figure 4: Modelled and parameterised quantities for Pine Island Glacier. (a-c) Melt rate, thermal driving, and sub-ice current speed from the model; (d-f) The same quantities for the best-fit parameterisation (18): d) Tuned parameterisation of melt rate; e) Tuned parameterisation of thermal driving as $(T^r - T_f^r)$; f) Tuned parameterisation of sub-ice speed as $(T^r - T_f^r)^{1/2} (\sin\theta)^{1/2}\, \Psi(3\ \mathrm{km})$.

https://doi.org/10.5194/egusphere-2026-2835
Preprint. Discussion started: 2 June 2026

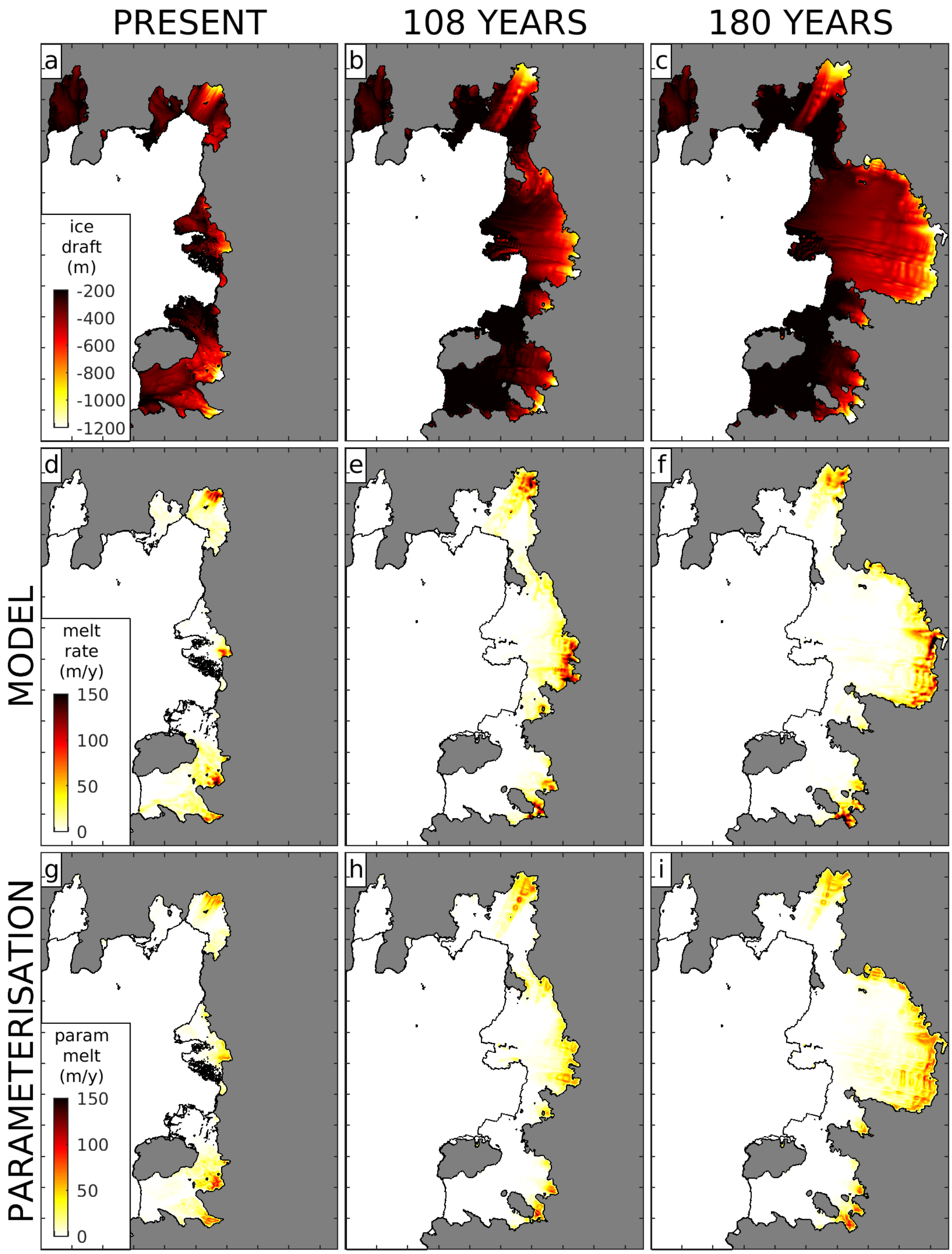

Figure 5: Modelled and parameterised melt rates for present and future ice geometries. (a-c) Ice draft for present day geometry and two future geometry snapshots from a simulation of Bett et al. (2024); (d-f) Modelled melt rates for these geometries; (g-i) Melt rates from the best-fit parameterisation (18) applied to these geometries.

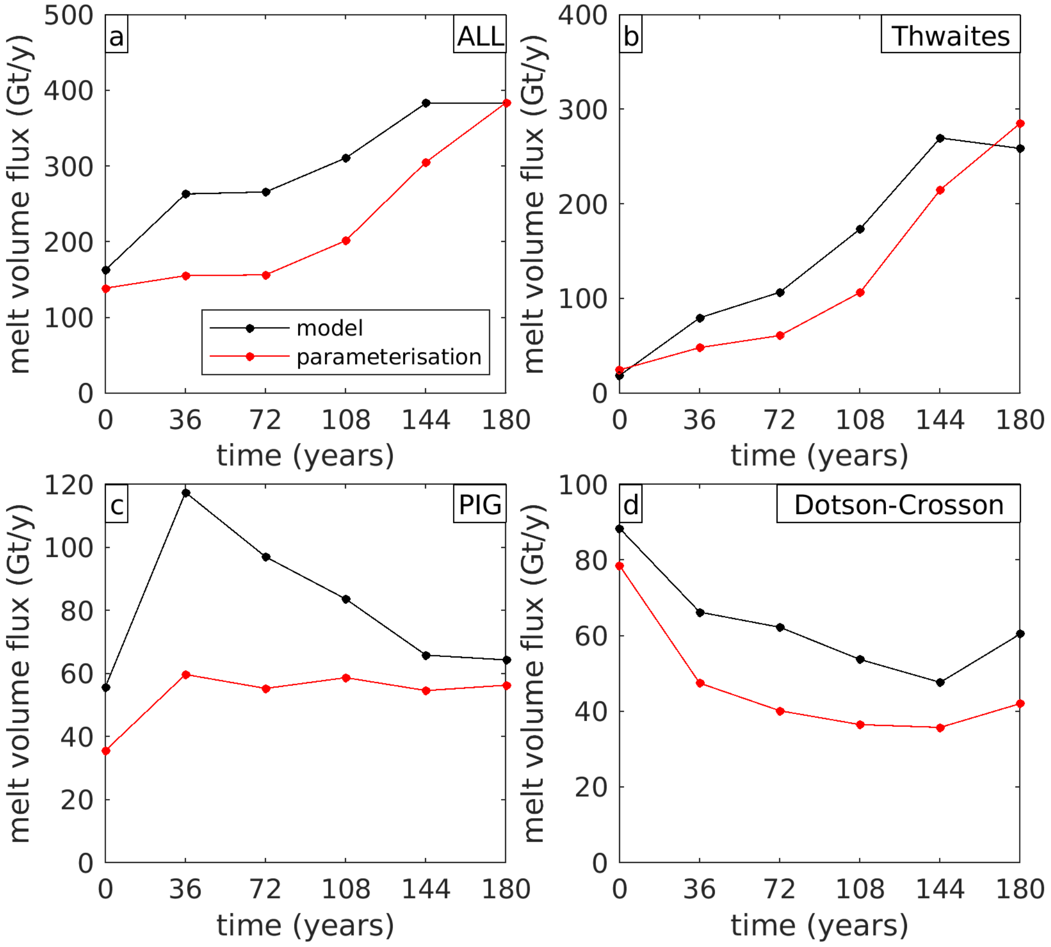

1035

Figure 6: Future evolution of modelled and parameterised melt rates as ice geometry evolves. (a) Evolution of total integrated meltwater flux for all ice shelves PIG—Dotson for present day geometry and five future snapshots from a simulation of Bett et al. (2024); (b-d) The same but separated into individual ice shelves.

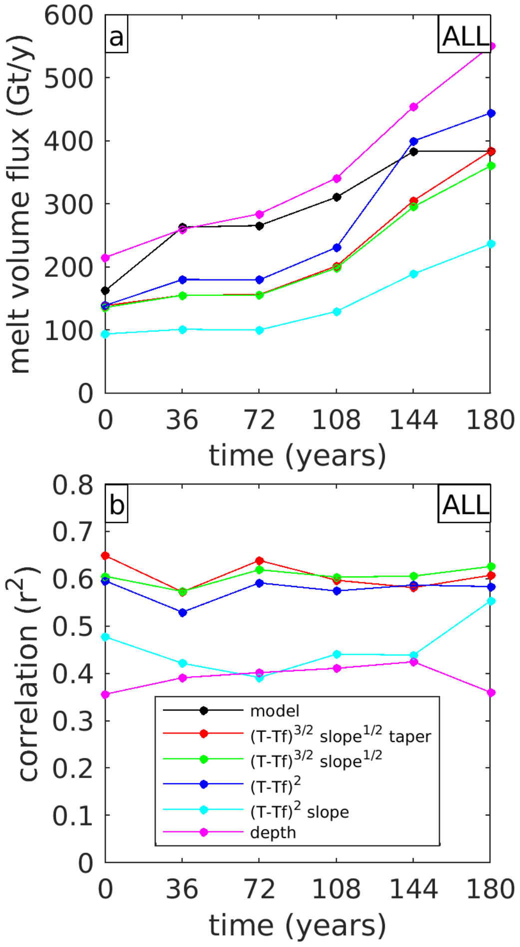

1040 **Figure 7: Performance of different parameterisations in capturing the future evolution of melt rates.** (a) Total meltwater flux for the model (black line) and five different melting parameterisations (coloured lines); (b) Spatial pattern correlation between the modelled melt pattern and the melt pattern predicted by each of the five parameterisations.

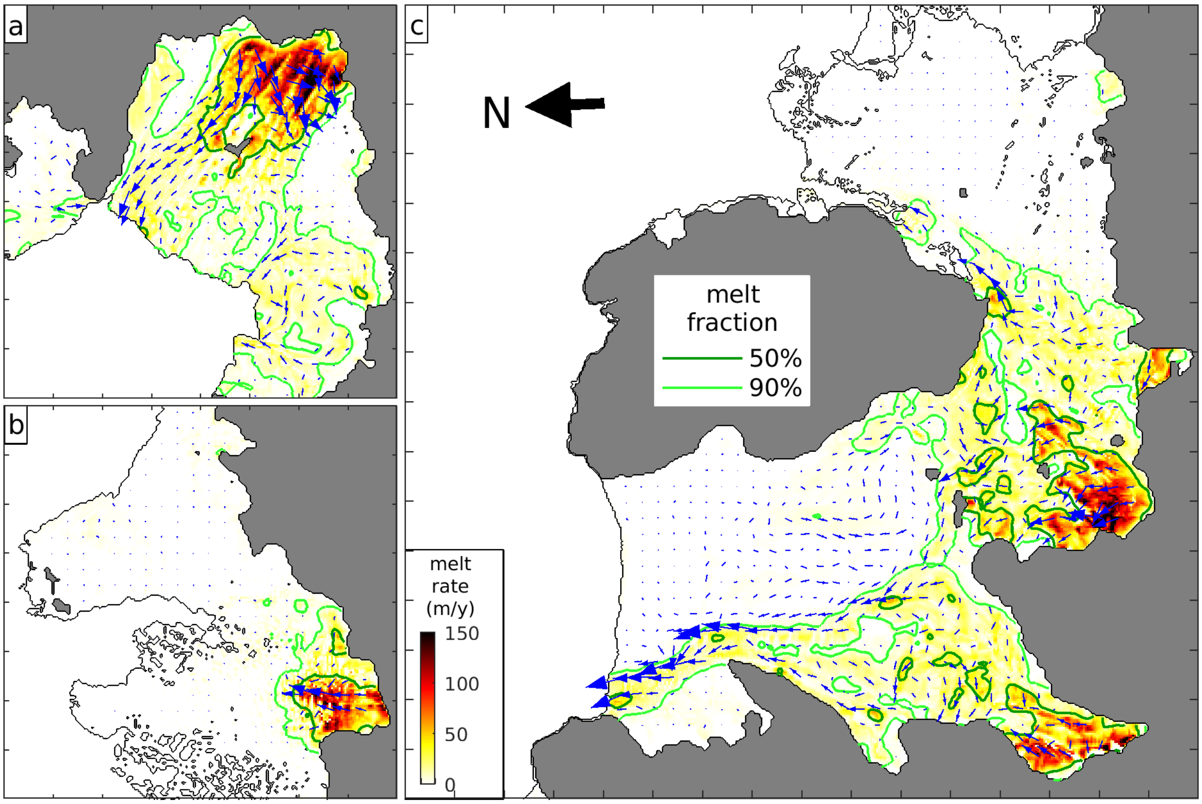

Figure 8: Relative importance of melting in deep 'hot spots' near grounding lines and shallower 'meltwater outflows'. Identical to
1045 Fig. 2d-f, but with contours enclosing 50% of the total meltwater flux (dark green) and 90% of the total flux (light green).

https://doi.org/10.5194/egusphere-2026-2835
Preprint. Discussion started: 2 June 2026

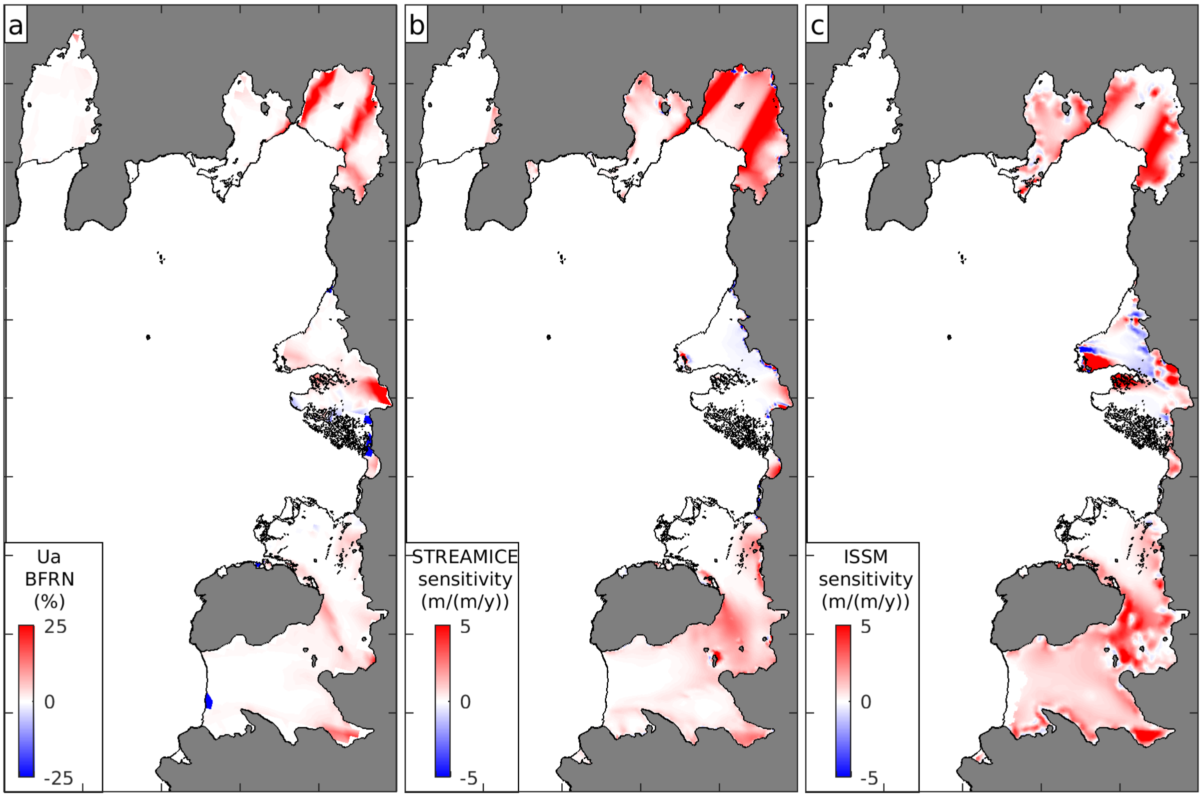

Figure 9: Sensitivity of grounded ice loss to melting in different locations from 3 different ice-sheet models. (a) Buttressing flux response number from the Úa model (Naughten et al., 2023). (b,c) Melting sensitivity maps from STREAMICE (Gourmelen et al., 2025) and ISSM (Morlighem et al., 2021).

1050